






Multiscale mechanical analysis of the elastic modulus of skin

Journal Article

Author(s):

[Wahlsten, Adam](#) ; [Stracuzzi, Alberto](#) ; [Lüchtfeld, Ines](#); [Restivo, Gaetana](#); [Lindenblatt, Nicole](#); [Giampietro, Costanza](#) ; [Ehret, Alexander Edmund](#) ; [Mazza, Edoardo](#) 

Publication date:

2023-10-15

Permanent link:

<https://doi.org/10.3929/ethz-b-000637402>

Rights / license:

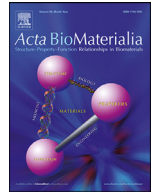
[Creative Commons Attribution 4.0 International](#)

Originally published in:

Acta Biomaterialia 170, <https://doi.org/10.1016/j.actbio.2023.08.030>

Funding acknowledgement:

179012 - Skin biomechanics and mechanobiology for wound healing and tissue engineering (SNF)
213498 - Skin stretch: unraveling the complexity of mechanotransduction across scales (SNF)



Full length article

Multiscale mechanical analysis of the elastic modulus of skin

Adam Wahlsten^a, Alberto Stracuzzi^{a,b}, Ines Lüchtfeld^c, Gaetana Restivo^d,
Nicole Lindenblatt^e, Costanza Giampietro^{a,b}, Alexander E. Ehret^{a,b}, Edoardo Mazza^{a,b,*}^a Institute for Mechanical Systems, Department of Mechanical and Process Engineering, ETH Zurich, Leonhardstrasse 21, Zurich 8092, Switzerland^b Empa, Swiss Federal Laboratories for Materials Science and Technology, Überlandstrasse 129, Dübendorf 8600, Switzerland^c Institute for Biomedical Engineering, Department of Information Technology and Electrical Engineering, ETH Zurich, Gloriastrasse 35, Zurich 8092, Switzerland^d Department of Dermatology, University Hospital Zurich, Zurich 8091, Switzerland^e Department of Plastic and Hand Surgery, University Hospital Zurich, Zurich 8091, Switzerland

ARTICLE INFO

Article history:

Received 28 May 2023

Revised 27 July 2023

Accepted 15 August 2023

Available online 19 August 2023

Keywords:

Atomic force microscopy

Elastic modulus

Extracellular matrix

Fiber network

Mechanical properties

Skin

Stiffness

ABSTRACT

The mechanical properties of the skin determine tissue function and regulate dermal cell behavior. Yet measuring these properties remains challenging, as evidenced by the large range of elastic moduli reported in the literature—from below one kPa to hundreds of MPa. Here, we reconcile these disparate results by dedicated experiments at both tissue and cellular length scales and by computational models considering the multiscale and multiphase tissue structure. At the macroscopic tissue length scale, the collective behavior of the collagen fiber network under tension provides functional tissue stiffness, and its properties determine the corresponding elastic modulus (100–200 kPa). The compliant microscale environment (0.1–10 kPa), probed by atomic force microscopy, arises from the ground matrix without engaging the collagen fiber network. Our analysis indicates that indentation-based elasticity measurements, although probing tissue properties at the cell-relevant length scale, do not assess the deformation mechanisms activated by dermal cells when exerting traction forces on the extracellular matrix. Using dermal-equivalent collagen hydrogels, we demonstrate that indentation measurements of tissue stiffness do not correlate with the behavior of embedded dermal fibroblasts. These results provide a deeper understanding of tissue mechanics across length scales with important implications for skin mechanobiology and tissue engineering.

Statement of Significance

Measuring the mechanical properties of the skin is essential for understanding dermal cell mechanobiology and designing tissue-engineered skin substitutes. However, previous results reported for the elastic modulus of skin vary by six orders of magnitude. We show that two distinct deformation mechanisms, related to the tension–compression nonlinearity of the collagen fiber network, can explain the large variations in elastic moduli. Furthermore, we show that microscale indentation, which is frequently used to assess the stiffness perceived by cells, fails to engage the fiber network, and therefore cannot predict the behavior of dermal fibroblasts in stiffness-tunable fibrous hydrogels. This has important implications for how to measure and interpret the mechanical properties of soft tissues across length scales.

© 2023 The Author(s). Published by Elsevier Ltd on behalf of Acta Materialia Inc.
This is an open access article under the CC BY license (<http://creativecommons.org/licenses/by/4.0/>)

* Corresponding author at: Institute for Mechanical Systems, Department of Mechanical and Process Engineering, ETH Zurich, Leonhardstrasse 21, 8092 Zurich, Switzerland.

E-mail address: mazza@imes.mavt.ethz.ch (E. Mazza).

1. Introduction

Mechanics plays a key role in determining the form and function of biological tissues [1]. An excellent example is the skin, the deformable and tear-resistant outer barrier of the human body that protects the vital inner organs from damage. Fulfilling this protective function requires both high compliance and extreme de-

fect tolerance to adapt to and sustain the mechanical forces exerted during normal physical activities without tearing [2]. External forces are borne primarily by the extracellular matrix (ECM) of the dermis, the main structural layer of the skin [3]. Its ECM is a complex composite material, which is composed of interstitial fluid, an entangled network of collagen fibers providing structural resistance, and charged proteoglycans controlling tissue hydration. The structural proteins of the ECM are also the primary attachment sites for dermal cells, which are able to exert forces on the ECM and thus sense their biophysical environment [4]. In fact, various mechanical cues are known to determine cell behavior [5–10], thereby influencing processes such as the repair and regeneration of wounded tissue [11]. Understanding the mechanical behavior of the skin is therefore important for a wide range of applications and processes across multiple length scales, such as the design of tissue-engineered skin-equivalent materials [12] and epidermal electronic devices [13], planning of reconstructive surgery [14], and the mechanobiology of aging [15] and wound healing [11].

In order to resolve the role of mechanics in these processes, one prerequisite is an accurate determination of the mechanical properties of the skin at the length scales of interest [12]. Although the mechanical behavior of the skin is highly nonlinear [16,17], anisotropic [17,18], and time dependent [16,19], essential information is still contained in a single metric of its material stiffness, the elastic (Young's) modulus E . However, values of the elastic modulus of skin reported in the literature span six orders of magnitude—from hundreds of Pa [20,21] to tens [17] and even hundreds of MPa [22,23] (Fig. 1a). To illustrate, six orders of magnitude difference in elastic modulus is comparable to the difference between the modulus of a typical rubber ($E \sim 1$ MPa [24]) and that of diamond ($E \sim 1000$ GPa [25]). In fact, large discrepancies in the elastic moduli reported exist not only for skin but also for several other soft biological tissues [26], indicating the difficulties associated with the measurement, analysis, and interpretation of the mechanical properties for this class of materials. A physical explanation of these discrepancies has not yet been proposed, but it has been hypothesized that the testing technique used and the tissue length scale probed influence the modulus measured [26,27], in conflict with the concept of E being a *material* property. In line with this hypothesis, a common conjecture is that tissue stiffness for applications in mechanobiology needs to be measured at the cell-perception scale using, for example, atomic force microscopy (AFM) [20,28–30]. However, direct experimental and theoretical support for this argument is lacking.

Here, we analyze the mechanical behavior of skin from the cellular to the tissue length scale through dedicated experiments in order to resolve these discrepancies. To rationalize the data, we develop a multiscale model of the human dermis, which takes the discrete structure of the collagen fiber network, the surrounding ground matrix, and their level of interconnection into account. We show that macroscopic tensile testing can be prone to overestimating the tissue-level elastic modulus *in vivo* due to the highly nonlinear strain-stiffening behavior arising from the progressive engagement of collagen fibers. In contrast, the fiber network does not contribute to the stiffness measured in AFM-based indentation. Instead, the indentation stiffness measured depends on the composition of the ground matrix. Moreover, the indentation stiffness measured is strongly influenced by the surface topography of the sample, leading to a general underestimation of the material stiffness and an apparent heterogeneity of the modulus measured. Based on our multiscale model, we therefore hypothesized that AFM-based indentation does not activate the deformation mechanism involved in ECM resistance to traction forces exerted by dermal cells. Using stiffness-tunable, dermal-equivalent collagen hydrogels, we demonstrate our hypothesis in that indentation mea-

surements of tissue stiffness at the cell-perception length scale fail to predict dermal fibroblast behavior.

2. Materials and methods

2.1. Skin biopsies

Human skin biopsies were obtained from the biobank of the dermatology department at University Hospital Zurich within the SKINTEGRITY.CH research program (EK 647 and EK 800). The skin biopsies were surplus tissue from female donors who underwent surgery and provided signed informed consent to use the skin for research purposes (Supplementary Table S3). The use of surplus skin for biomechanical experiments had been approved by the Ethical Commission of Canton Zurich (BASEC ID: 2017-00684). Skin from three donors (donor 1: 39 years of age, breast skin; donor 2: 32, breast; donor 3: 43, abdomen) were used for the measurement of mechanical properties in uniaxial (UA) tension, microindentation, and AFM indentation (Fig. 1). Biopsies from four additional donors (donor 4: 68, abdomen; donor 5: 22, breast; donor 6: 43, breast; donor 7: 44, abdomen) were used to characterize the mechanical behavior under equibiaxial tension (Fig. 2f). Human skin tissue was kept in Dulbecco's modified Eagle medium (DMEM; low glucose, Gibco) supplemented with 1% penicillin–streptomycin (P0781, Sigma) at 4 °C until sample preparation for mechanical testing, which was performed within 24 h of biopsy collection.

Mouse skin biopsies were obtained from adult (7–8 weeks old) wild-type C57BL/6 male mice. The mice were housed in accordance with Swiss animal protection guidelines and were sacrificed in an unrelated study. The backs of the mice were shaved, and the entire back skin was excised carefully. Murine skins were kept in DMEM on ice until sample preparation for mechanical testing, which was performed on the same day as animal sacrifice.

Both human and murine skin biopsies were placed on a graduated mat, and specimens for UA testing with dimensions 40 mm \times 5 mm (gauge dimensions: 20 mm \times 5 mm) were cut with a razor blade. We note that the orientation of the human skin biopsies with respect to the body directions was unknown. Excess fat was removed, such that the specimens contained only the epidermal and dermal layers. For the murine skin samples, specimens for UA testing were cut either in the cranio–caudal or the mediolateral direction to assess the influence of in-plane anisotropy. Note that, in addition to dermis and epidermis, the murine skin also contains adipose tissue and a thin layer of subcutaneous muscle (*Panniculus Carnosus*).

Tissue pieces adjacent to the samples cut for UA tension tests were washed in phosphate-buffered saline solution (PBS; Gibco), quickly dried on tissue paper to remove excess water, embedded in optimal cutting temperature compound (Tissue-Tek, Sakura), and finally snap-frozen in liquid-nitrogen-cooled isopentane. Snap-frozen samples were stored at -80 °C. Through-thickness cryosections were prepared for AFM experiments (50 μ m thickness) and histology (15 μ m) using a cryotome, whereas 2 mm through-thickness sections were cut with a surgical scalpel for microindentation tests. Previous work has demonstrated that the snap-freezing procedure does not affect the tissue properties measured [20].

2.2. Silicone elastomers

To validate the mechanical testing techniques on a soft, isotropic material that is expected to be homogeneous at the length scales considered, we fabricated samples of a polydimethylsiloxane (PDMS) silicone elastomer [31,32]. PDMS (Sylgard 184, Dow Corning) was mixed at a base-to-crosslinker ratio of 35:1 (w/w). The mixture was degassed in a vacuum desiccator, cast into

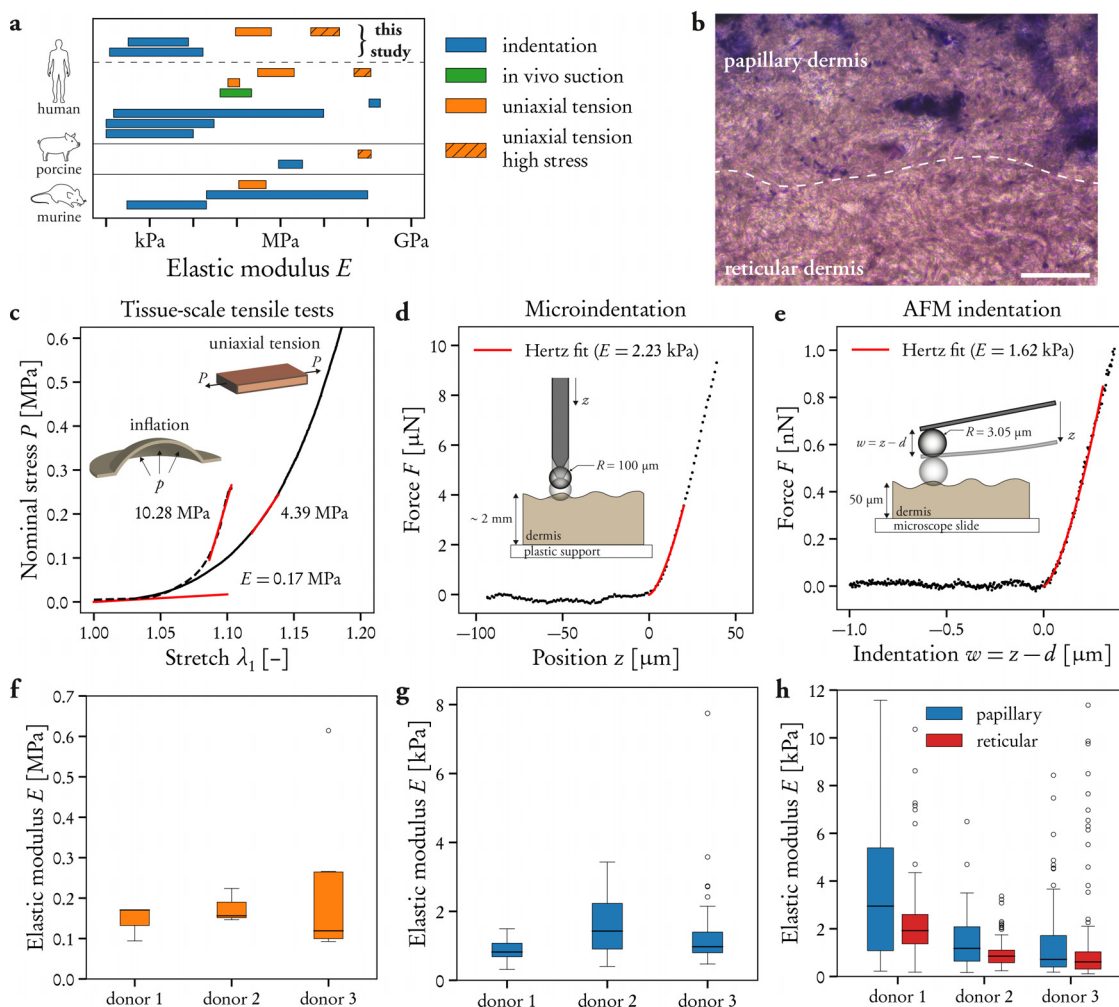


Fig. 1. Mechanical properties of human skin across length scales. (a) Ranges of elastic moduli of human, murine, and porcine skin reported in literature and measured in this study using different testing techniques (indentation, uniaxial tension, and *in vivo* suction). (b) Histological cross-section of the human dermis, showing the cell-dense papillary layer (top) and the sparsely populated reticular layer (bottom), composed of thick fiber bundles. White dashed line indicates the layer boundary. Scale bar: 100 μm . (c–e) Representative uniaxial tension and membrane inflation (c), microindentation (d), and AFM indentation (e) experiments on healthy human skin tissue. Figure insets show schematics of the measurement techniques. (f–h) Elastic moduli of human dermal tissue measured for three donors in UA tension (f; $n = 3, 3, 7$), microindentation (g; $n = 32, 36, 38$), and AFM indentation (h; $n = 125, 131, 59, 107, 94, 126$). Boxes extend from the lower to the upper quartile of the data, with a line at the median and whiskers extending to $1.5 \times$ the interquartile range.

petri dishes, degassed again, and finally cured in an oven for 4 h at 60 °C. Mechanical testing was performed strictly on the day after elastomer preparation to reduce the effect of aging [31,32].

2.3. Cell culture and collagen hydrogel preparation

Primary human dermal fibroblasts (FBs) were isolated in our previous study [8] or obtained commercially (C-013-5C, Gibco). FBs were cultured in DMEM⁺⁺⁺ (DMEM low glucose, Gibco; supplemented with 10% fetal bovine serum (Gibco), 1% penicillin-streptomycin, and 1% HEPES (1M, Sigma)) at 37 °C and 5% CO₂ and harvested at passage three to four.

Collagen hydrogels were prepared as described previously [8,33]. Briefly, FBs were counted and resuspended in DMEM⁺⁺⁺ at a concentration of 1.1×10^5 ml⁻¹. For a final gel volume of 3 ml, 0.4 ml cell suspension was mixed thoroughly with 0.6 ml neutralizing buffer and 2 ml ice-cold acidified type I bovine collagen (5 mg ml⁻¹, Symatase). Control gels were produced by casting the gel mixture into 6-well inserts (353091, Corning), after which they were allowed to solidify for 15 min in an incubator (37 °C, 5% CO₂). To create (compressed) gels of higher collagen concentration, some of the gels cast were plastically compressed by means of custom-

designed 3D-printed stamps and a stainless steel weight to a final thickness of 0.5 mm. The volume fraction of collagen in control and plastically compressed gels was calculated as 0.23% and 3.36%, respectively, using a mass density of 1.42 g ml⁻¹ for collagen [34]. For biological assays, the cell-containing hydrogels were cultured in DMEM⁺⁺⁺ for seven days prior to fixation, with medium change every two to three days. For mechanical testing, acellular versions of the hydrogels were prepared and cultured in DMEM⁺⁺⁺ as described above. Mechanical tests were performed three days after gel preparation.

2.4. Histology and immunofluorescence microscopy

Skin cryosections were thawed, washed, fixed in 4% paraformaldehyde (PFA; 28908, ThermoFisher Scientific) for 15 min, and stained with hematoxylin and eosin (H&E; ab245880, Abcam) according to the manufacturer's protocol. Micrographs were acquired using a Nikon Eclipse Ts2 microscope equipped with a 4X or a 20X objective.

Whole-mount immunofluorescence stainings of collagen hydrogels were performed as described previously [8]. Briefly, collagen hydrogels were fixed in 4% PFA at 4 °C overnight and subsequently

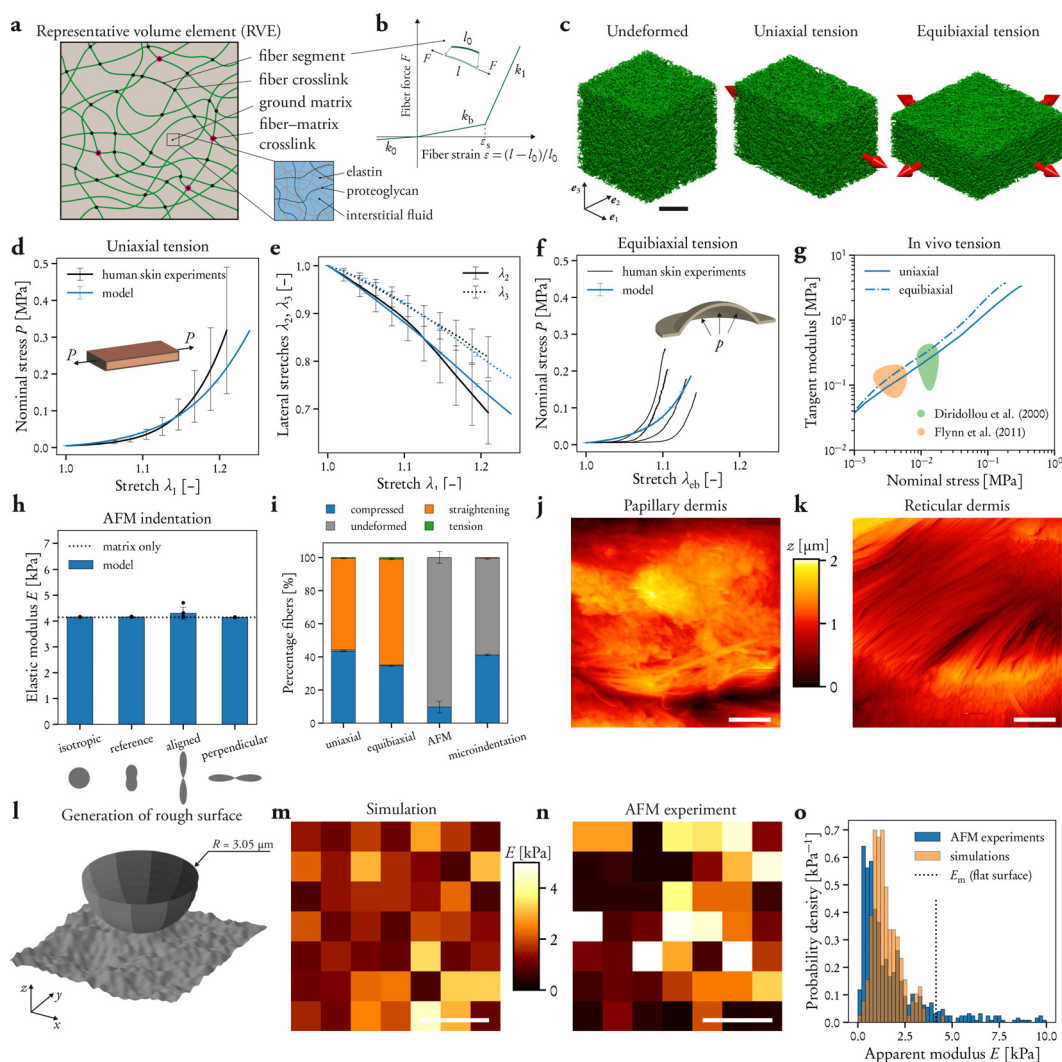


Fig. 2. Multiscale model of the human dermis. (a) A representative volume element (RVE) is modeled as a composite of a discrete network of collagen fibers (green) embedded in a soft, hydrated ground matrix (beige). Entanglement between the fiber network and the ground matrix is represented by fiber–matrix crosslinks (magenta). (b) A trilinear force–strain law is used to model the elastic behavior of slender fiber segments, with compressive stiffness k_0 , unbending stiffness $k_b > k_0$, and tensile stiffness $k_1 \gg k_0$ for a taut fiber segment ($\varepsilon > \varepsilon_s$). (c) Rendering of the undeformed fiber network microstructure (left) and upon uniaxial (middle) and equibiaxial (right) stress. Scale bar: 100 μm . (d–g) The model is fitted to uniaxial stress–stretch (d) and kinematics (e) data [16], and is in good agreement with membrane inflation experiments (f) and *in vivo* data (g; refs. [39,40]). In g, solid and dash-dotted lines represent model predictions for uniaxial and equibiaxial stress states, respectively. (h) Model prediction of the influence of fiber network orientation on AFM indentation modulus. (i) Distribution of fiber strain in representative uniaxial tension, equibiaxial tension, AFM indentation, and microindentation simulations. (j, k) Representative AFM contact mode topography images of hydrated human papillary (j) and reticular (k) dermis. Note the presence of fiber bundles in the reticular dermis (k), whereas the cross-section surface of the papillary dermis appears more diffuse (j). The color bar applies to both images. Scale bars: 2 μm . (l) Representative 10 $\mu\text{m} \times 10 \mu\text{m}$ patch of a rough, random surface. The AFM indenter is shown for reference. (m, n) Representative surface distributions of the elastic modulus computed by indentation simulations on a rough, random surface (m) versus measured with the AFM (n). The color bar applies to both images. Scale bars: 10 μm . (o) Distribution of elastic modulus measured by AFM indentation ($n = 642$) and reproduced by corresponding simulations on random surfaces ($n = 193$ simulations from 4 random surfaces). The dotted vertical line denotes the equivalent elastic modulus E_m of the ground matrix for a flat surface, cf. h.

washed in PBS/0.3% Triton-X (PBS-TX) for 6 h. Samples were blocked for 2 h in 10% bovine serum albumin dissolved in PBS-TX, after which they were incubated with the primary antibody at 4 °C overnight. Thereafter, samples were washed thoroughly in PBS for at least 24 h, after which antibody incubation was repeated with the secondary antibody. The following antibodies and dilutions were used: mouse anti-Ki67 (1:100; BD550609, BD Biosciences), rabbit anti-mouse IgG (H&L) Alexa Fluor 555 (1:400; A27028, Invitrogen). F-actin was visualized using TRITC-conjugated rhodamine phalloidin (R415, Invitrogen). Cell nuclei were counterstained with DAPI (1:1000; 62248, ThermoFisher Scientific). Gel samples were mounted on glass slides with Fluoroshield mounting medium (F6182, Sigma), and widefield micrographs were acquired with an inverse spinning-disk confocal microscope (Nikon Eclipse Ti-E) equipped with a 10X objective.

For quantification of cell proliferation and spreading area, z-stacks of at least 400 μm thickness were analyzed. Cell nuclei and Ki67-positive nuclei were counted manually, and the projected cell area was calculated by manually segmenting each cell using the freehand area selection tool in ImageJ. Cells close to each other where individual outlines could not be distinguished were excluded. Images were only adjusted for brightness and contrast.

2.5. Mechanical testing

2.5.1. Atomic force microscopy

AFM-based indentation tests were performed using a Flex-Bio AFM (Nanosurf). The AFM scanhead was mounted on top of an inverted microscope (Zeiss Axio Observer or Nikon Eclipse Ti-E), which provided optical access to the sample surface and the can-

tilever position. All samples were immersed in PBS during testing to provide physiological hydration and to eliminate attractive capillary forces between the sample surface and the probe tip. The sample surface was probed using soft cantilevers (0.1 nN nm^{-1} ; CP-qp-CNT-PS-C, Nanosensors) with a $6.1 \text{ }\mu\text{m}$ diameter polystyrene colloidal particle attached to the cantilever tip. Prior to testing, the cantilever spring constant k was measured using the Sader method as implemented in the AFM control software (C3000, Nanosurf), and the deflection sensitivity of the photodiode was calibrated in PBS by indenting a rigid glass surface.

Force–distance curves were acquired in force spectroscopy mode with an indentation speed of $1 \text{ }\mu\text{m s}^{-1}$. A minimum of three $30 \text{ }\mu\text{m} \times 30 \text{ }\mu\text{m}$ locations per sample were probed; at each location, 7×7 positions were indented, and the locations were separated by at least $500 \text{ }\mu\text{m}$. For experiments on hydrated human and murine skin cryosections, the cantilever was guided over both the papillary and the reticular layer of the dermis, as identified from the brightfield channel, and force–indentation curves were acquired over each layer separately.

Additional AFM indentation experiments were performed with human dermis either exposed to a hypotonic solution ($0.1 \times$ PBS) to induce tissue swelling or after treatment with the enzyme hyaluronidase. For the swelling experiments, dermal cross-sections were first tested in PBS as described above. After data acquisition was completed, the scanhead was removed and the immersion solution was exchanged to $0.1 \times$ PBS. AFM experiments were then repeated on the swollen tissue after 15 min of incubation. Separate tissue cross-sections were used for the hyaluronidase experiments. Following control measurements in PBS, the scanhead was removed and the tissue was incubated for 60 min in a 0.5 mg ml^{-1} hyaluronidase solution (Type I-S, H3506, Sigma) [35,36]. After washing in PBS, AFM indentation experiments were repeated on the digested tissue.

To extract the apparent modulus E from AFM force–distance curves, the cantilever deflection d and piezo position z were first converted to force $F = kd$ and indentation $w = z - d$, respectively. Force–distance curves without a clear contact point were discarded. Next, a constrained sequential search algorithm (cf. ref. [37]) was implemented to find the contact point and the corresponding elastic modulus from each F – w -curve. To this end, each data point w_i is sequentially taken as the trial contact point w^* , and the elastic modulus E^* for this assumed contact point is obtained by fitting the Hertzian contact solution for a rigid, spherical indenter and a flat, elastic half-space [37] to the data, that is,

$$F = \frac{4}{3} \frac{E^*}{1 - \nu^2} \sqrt{R} \delta^{3/2}. \quad (1)$$

Here, ν denotes Poisson's ratio, R is the radius of the indenter, and $\delta = w - w^*$ is the indentation depth. Finally, the elastic modulus E and the corresponding contact point were taken as the pair that provided the best fit of the data. The fitting procedure is illustrated in Supplementary Fig. S4. For the purpose of extracting an apparent modulus and for consistency with literature, a Poisson's ratio $\nu = 0.5$ was used. Therefore, the E obtained from indentation tests should be interpreted as the apparent modulus of an equivalent isotropic, incompressible material. However, we emphasize that the computational model used to rationalize the experiments does not represent skin as an incompressible solid [38], see Section 2.7.

2.5.2. Microindentation

Microindentation tests were performed with a micromechanical testing system (FT-MTA02, FemtoTools) by adapting a testing protocol previously developed for soft elastomers [32]. Briefly, high-precision spheres (Sandoz Fils SA) manufactured out of cubic zirconia ($200 \text{ }\mu\text{m}$ diameter, grade G10) or ruby ($1000 \text{ }\mu\text{m}$ diameter,

grade G25) were glued using a UV-light-cure adhesive (AA3494, Loctite) to the end of force-sensing probes (FT-S1000, FemtoTools), which have a range of $\pm 1000 \text{ }\mu\text{N}$ and a sensitivity of $0.05 \text{ }\mu\text{N}$. The system compliance ($0.0012 \text{ }\mu\text{m }\mu\text{N}^{-1}$) is negligible (cf. Fig. 1d). Samples for microindentation testing were glued to the bottom of a petri dish using cyanoacrylate glue and immersed in PBS during testing. The PBS used was mixed thoroughly with a small drop of kitchen detergent (per 50 ml PBS) to reduce the surface tension of the liquid, which otherwise exerts spurious forces on the shaft of the force-sensing probe. Force–distance curves were acquired in stepping mode at a displacement rate of $5 \text{ }\mu\text{m s}^{-1}$. From the force–distance data, the apparent modulus was extracted with the same method as outlined above for AFM indentation.

2.5.3. Uniaxial testing

UA tension tests were performed as described previously [16]. Testpieces were clamped to two axes of a custom-built testing rig (MTS Systems), comprised of horizontal hydraulic actuators, 50 N force sensors, and a CCD camera (Pike F-100B, Allied Vision Technologies), equipped with a $0.25 \times$ telecentric lens (NT55-349, Edmund Optics), which captures top-view images of the deforming testpieces. The samples were immersed in physiological saline solution (0.9% NaCl) during testing and elongated at a nominal strain rate of 0.001 s^{-1} . Based on our previous work on the time- and history-dependent mechanical behavior of human and murine skin [16], we selected the strain rate low enough that the response observed was representative of the long-term tissue behavior. The nominal stress was calculated as $P = F/(WH)$, where F is the force measured, W is the reference width of the sample, and H is the thickness in the undeformed state (Supplementary Table S3). For the skin biopsies, the thickness was estimated from images of histological cross-sections, whereas for collagen hydrogels and PDMS elastomers, the thickness was measured using a brightfield microscope (LSM 5 Pascal, Zeiss). The local in-plane principal stretches, λ_1 and λ_2 , were extracted from the sequence of top-view images by tracking the displacement of fiducial markers in the center of the testpiece using a custom-written optical flow tracking algorithm [31]. The elastic modulus E was defined as the initial slope of the stress–stretch curve, which was calculated by a linear fit of the stress–stretch data up to 2% linear strain. The tangent modulus $E'(\lambda_1) = \partial P / \partial \lambda_1$ was computed as a measure of stiffness at larger stretches.

Due to the soft and highly nonlinear behavior of the skin, the identification of a zero-stress reference state in ex vivo tension experiments is complicated. In line with our previous work [16], a small threshold stress $P_{\text{th}} = 5 \text{ kPa}$ was used to define the experimental reference criterion (Supplementary Note S1.1, Fig. S1b). Note that this is required to ensure that the sample is taut [16], and the magnitude is within the range of estimates of the *in vivo* skin tension (1 kPa to 18 kPa [39,40]; see Supplementary Table S2). In contrast, a clear transition point between the initial, bending-dominated alignment phase, during which the slack sample becomes taut, and the subsequent stretching phase can be identified in the force–displacement curves for collagen hydrogel and PDMS samples, which was used as a reference criterion for these materials, cf. Supplementary Fig. S1c.

2.5.4. Equibiaxial testing

The equibiaxial response of human skin was characterized using a custom-made membrane inflation setup [8,31]. Briefly, circular samples of approximately 45 mm diameter (abdominal skin) or 25 mm (breast skin) were cut with a surgical scalpel and fixed between two concentric, annular clamps (free diameter 30 mm or 18 mm), epidermal side facing up. The clamps were fastened on top of an inflation chamber, which was subsequently infused with physiological saline solution to inflate the sample by means of a

syringe pump (PhD Ultra, Harvard Apparatus). The syringe pump actuation was controlled by a LabView (National Instruments) code to achieve a pressure-controlled inflation of the sample at a pressure rate of 0.1 kPa s^{-1} . The inflation pressure p was measured with a pressure sensor (LEX 1, Keller), and top- and side-view images of the bulging membrane were captured using CCD cameras (GRAS-14S5C-C, Point Grey Research). The top camera was equipped with a telecentric lens to eliminate the zoom effect arising from the vertical motion of the inflating sample. The top- and side-view image sequences were used to measure the in-plane principal stretch $\lambda_{\text{eb}} = \sqrt{\lambda_1 \lambda_2}$ and the radius of curvature r at the apex of the sample, respectively. The equibiaxial Cauchy stress was approximated using Laplace's law, $\sigma_{\text{eb}} = pr/(2H\lambda_3)$ [31]. Since the stretch in thickness direction, λ_3 , is not measurable in this setup, the Cauchy stress was converted to nominal stress, $P = \lambda_{\text{eb}}\lambda_3\sigma_{\text{eb}} = \lambda_{\text{eb}}pr/(2H)$ (Fig. 2f). Note also that this corresponds to a homogenized stress across the tissue thickness; that is, the effect of bending is neglected.

2.6. Measurement of surface topography

To measure the surface topography of dermal cryosections used for AFM indentation, we imaged $10 \mu\text{m} \times 10 \mu\text{m}$ surface regions at 256×256 pixel resolution using the AFM in contact mode. Prior to imaging, the samples were fixed in glutaraldehyde (2.5% in PBS) and washed thoroughly with filtered PBS. AFM imaging was performed in PBS using cantilevers with a circular-symmetric tip shape ($<10 \text{ nm}$ nominal tip radius; qp-SCONT, Nanosensors). Image quality was optimized by tuning the set point (0.25 nN) and the feedback gains until trace and retrace lines coincided. Topography images were corrected for plane tilt and displayed as heat maps using perceptually uniform colormaps (Fig. 2jk).

The surface topography of hydrated skin sections used for microindentation testing was measured using a 3D laser scanning confocal microscope (VK-X250, Keyence) equipped with a 20X objective (Supplementary Fig. S16). The surface height was scanned with a $0.5 \mu\text{m}$ step size in z -direction. An area of $500 \mu\text{m} \times 500 \mu\text{m}$ in the dermis was analyzed. The height data obtained were corrected for plane tilt, smoothed with an S-filter, and the root-mean-square (RMS) height S_q was computed using Keyence Multi-FileAnalyzer software.

2.7. Computational models

Based on our previous work [38,41,42], we model the long-term equilibrium behavior of the human dermis and dermal-equivalent collagen hydrogels by combining a discrete representation of the collagen fiber network and a hyperelastic continuum description of the ground matrix (Fig. 2a). The simplification to only consider the dermal layer in the model for human skin is motivated by UA tension experiments comparing the behavior of full-thickness skin with that of dermis and epidermis individually after enzymatic digestion of the basement membrane, see Supplementary Note S2. Because the experiments were performed at low strain rates and small Péclet numbers, time-dependent viscoelastic and poroelastic contributions to the tissue response are neglected in our model formulation [38].

2.7.1. Fiber network generation

The collagen fiber network is modeled as a set of slender fibers, which intersect and interact mechanically at crosslinks [43]. The average coordination number of the fiber network is $\langle z \rangle = 4$, representing the formation of a crosslink between two longer fibers. We assume that crosslinks transmit forces but not moments, and that they are distributed randomly and uniformly throughout a representative volume element (RVE) of the tissue.

The procedure for generating three-dimensional discrete fiber networks consists of three principal steps, cf. refs. [41,43]. First, fiber crosslinks are seeded randomly in a cuboid domain of side length $s + 2l_{\text{max}}$ at the density ρ_c . Here, s denotes the size of the computational domain and l_{max} is the maximum length of a fiber segment. Next, each crosslink is connected to four of its neighbors. We define a fiber segment as the line segment connecting two crosslinks. For each crosslink, we identify fiber segments by a random weighted choice process, sampling among its neighboring crosslinks located within a sphere of radius l_{max} . The weight associated with a potential fiber segment of length l , in-plane angle ϕ , and out-of-plane angle θ is taken to be proportional to $p(l, \phi, \theta) = p_l(l)p_\phi(\phi)p_\theta(\theta)$, where $p_l(l)l^2 dl$, $p_\phi(\phi)d\phi$, and $p_\theta(\theta)\sin\theta d\theta$ represent the corresponding probability density elements (see ref. [44], pp. 67–69). Equivalently, the fiber statistics can be described in terms of the probability density functions $f_l(l) = p_l(l)l^2$, $f_\phi(\phi) = p_\phi(\phi)$, and $f_\theta(\theta) = p_\theta(\theta)\sin\theta$, which satisfy the normalization criterion

$$\int_0^{l_{\text{max}}} \int_0^{2\pi} \int_0^\pi f_l(l)f_\phi(\phi)f_\theta(\theta) d\theta d\phi dl = 1. \quad (2)$$

Here, a gamma distribution with shape parameter α and scale parameter $\beta = 1 \mu\text{m}$ is chosen for the fiber lengths, such that the mean fiber length equals $l_c = \alpha\beta$. To avoid generating arbitrarily long fibers, the gamma distribution is cropped at l_{max} and renormalized. The distribution of fiber in-plane and out-of-plane angles is prescribed by a girdle-type Dimroth–Watson orientation distribution with concentration parameter κ [45]; this results in a transversally isotropic network with fibers concentrated around the membrane plane. Note that we here neglect possible in-plane anisotropy because no information on the orientation of the skin biopsies with respect to the body axes was available. Nonetheless, by varying the orientation distribution, a wide range of network architectures can be generated; the probability density functions used for generating various network microstructures are documented in Supplementary Table S4 and illustrated in Supplementary Fig. S5.

Finally, fiber segments outside the computational domain are removed, and fiber segments intersecting the boundaries are cropped to the intersection point. Since these fibers are cropped along their axis, their length is reduced but their orientation is preserved. To visualize the networks generated, the open-source ray-tracing software POV-Ray (version 3.7, Persistence of Vision Raytracer Pty. Ltd.) was used.

2.7.2. Matrix–network coupling

The ground matrix, composed of interstitial fluid and the remaining solid constituents, is modeled as a continuum, which is interconnected with the collagen fiber network at a subset of the fiber network crosslinks (Fig. 2a) [42]. Here, we consider the matrix and the network to be only weakly entangled and thus deform independently (no coupling). This assumption is based on a multiscale comparison with a model for which the phases are strongly coupled at the length scale of the fiber network crosslink-to-crosslink distance (Supplementary Results and Discussion S5.5). This latter case is implemented by including all internal fiber network crosslinks in the set of nodes used to mesh the ground matrix. In the case of no matrix–network coupling, no internal fiber network crosslinks are included in the matrix mesh.

2.7.3. Constitutive models

The mechanical behavior of slender, rope-like collagen fibers is represented phenomenologically by a trilinear force–strain relationship for the fiber segments (Fig. 2b) [41]. The fiber segments are assigned a low stiffness k_0 under compression ($\varepsilon < 0$), a stiffness $k_b > k_0$ in the straightening regime ($0 < \varepsilon \leq \varepsilon_s$), and a high

stiffness $k_1 \gg k_0$ once the fiber segment becomes taut ($\varepsilon > \varepsilon_s$). Here, the fiber strain is defined as $\varepsilon = (l - l_0)/l_0$, with l and l_0 being the current and reference length of the fiber segment, respectively.

We describe the long-term equilibrium behavior of the ground matrix by a compressible neo-Hookean model superposed with the Donnan osmotic pressure that arises due to fixed charged groups associated with the proteoglycans [42]. Thus, for a local state of deformation characterized by the deformation gradient \mathbf{F} , the left Cauchy–Green deformation tensor $\mathbf{b} = \mathbf{F}\mathbf{F}^T$, and the volume ratio $J = \det \mathbf{F}$, the strain-energy density in the matrix reads

$$\Psi_m = \frac{c}{2} \left[(\text{tr} \mathbf{b} - 3) + \frac{1}{m} (J^{-2m} - 1) \right] + \Psi_{\text{osm}}(J), \quad (3)$$

where c and m are material parameters and Ψ_{osm} is the strain-energy density associated with the osmotic pressure [46]. Accordingly, the Cauchy stress in the matrix is computed as

$$\boldsymbol{\sigma}_m = \frac{2}{J} \frac{\partial \Psi_m}{\partial \mathbf{b}} \mathbf{b} = \frac{c}{J} (\mathbf{b} - J^{-2m} \mathbf{I}) - \Delta \pi(J) \mathbf{I}, \quad (4)$$

where \mathbf{I} is the identity tensor and the Donnan osmotic pressure $\Delta \pi(J) = -\partial \Psi_{\text{osm}} / \partial J$ is given by Ehlers et al. [46]

$$\Delta \pi(J) = R_g \Theta \left(\sqrt{c_{\text{fc}}(J)^2 + 4c_{\text{ext}}^2} - 2c_{\text{ext}} \right) - \pi_0, \quad (5)$$

$$c_{\text{fc}}(J) = c_{\text{fc}}^{\text{ref}} \frac{1 - \varphi_s^{\text{ref}}}{J - \varphi_s^{\text{ref}}}.$$

Herein, R_g is the ideal gas constant, Θ is the absolute temperature, c_{fc} is the fixed charge concentration ($c_{\text{fc}}^{\text{ref}}$ being its value in the reference configuration), c_{ext} is the NaCl concentration in the external bath, φ_s^{ref} is the reference solid volume fraction, and π_0 is a constant to ensure a stress-free reference configuration.

2.7.4. Material parameters

The volume fraction of collagen in the tissue, φ_{col} , is related to the topology of the fiber network. In fact, for a fiber network with a crosslink density ρ_c , an average nodal coordination number $\langle z \rangle$, and average fiber segment length l_c and diameter d_f , the collagen volume fraction follows approximately as [47]

$$\varphi_{\text{col}} = \rho_c \frac{\langle z \rangle}{2} l_c \pi \frac{d_f^2}{4}. \quad (6)$$

For human dermis, we assume a water content $\varphi_{\text{F}}^{\text{ref}} = 1 - \varphi_s^{\text{ref}} \sim 70\%$ [48] and a collagen content of 75% per dry tissue weight [49], yielding a collagen volume fraction of $\varphi_{\text{col}} = 22\%$. Based on scanning electron microscopy (SEM) images of papillary dermis [50], we take an approximate average fiber segment length $l_c = 20 \mu\text{m}$, from which the fiber diameter and the crosslink density were chosen according to Eq. (6) as $2.37 \mu\text{m}$ and $1.275 \times 10^{-3} \mu\text{m}^{-3}$, respectively. The fiber stiffness in unbending k_b and tension k_1 , the fiber slackness ε_s , the concentration parameter of the fiber out-of-plane orientation κ , and the matrix shear stiffness c were tuned to match data from our previous UA tension experiments on human skin [16]. In particular, κ governs the ratio between in-plane and out-of-plane lateral contraction, c influences the overall compressibility but has little effect on the uniaxial stress, and k_1 , k_b , and ε_s determine the shape and magnitude of both the stress and the lateral contraction [38]. In the model comparison with UA and equibiaxial data, we take into account the threshold stress P_{th} used to define the reference configuration in experiments, see ref. [38] for details. The fixed charge concentration $c_{\text{fc}}^{\text{ref}} = 25 \text{ mM}$ was chosen according to ref. [16].

For the collagen hydrogels, the volume fraction of collagen is known from the material composition (Section 2.3). Based on SEM images (cf. Fig. 3a, ref. [51]), we take a representative average fiber segment length $l_c = 5 \mu\text{m}$ and a fiber diameter $d_f = 150 \text{ nm}$. The

crosslink density for the control gels is thus computed from (6) as $\rho_c = 0.013284 \mu\text{m}^{-3}$. The fiber orientation distribution is assumed isotropic. Finally, due to the large aspect ratio and straightness of the fibers (Fig. 3a), we set the compressive stiffness $k_0 = 0 \mu\text{N}$ and the fiber slackness $\varepsilon_s = 0$. The fiber stiffness in tension and the shear stiffness of the matrix are then tuned to match the UA tension and kinematics data (Supplementary Fig. S6ef). Because of the lack of fixed charges in the collagen hydrogel, the Donnan contribution (5) to the matrix stress (4) is neglected.

The material parameters for compressed hydrogels are derived directly from the control hydrogels and simulations of the compression process without further parameter fitting, see Supplementary Methods S4.3.2 and Supplementary Fig. S6. A summary of all material parameters used can be found in Supplementary Table S5.

2.7.5. Numerical simulations

The algorithms and data structures for generating fiber networks, meshing and coupling the matrix, and preparing finite element models are written in Python (version 3.7.6, Python Software Foundation), making use of the open-source scientific computing packages NumPy, SciPy, and Numba. Mechanical boundary value problems are solved using the implicit solver in Abaqus/Standard (Abaqus 6.14-1, Dassault Systèmes), with the constitutive model for the matrix implemented as a user-defined material (UMAT). Fiber segments are discretized with axial connector elements (CONN3D2), whereas linear tetrahedral elements (C3D4) are used for the matrix. Further details on the fiber network model, including numerical stabilization methods and an RVE size convergence analysis, are reported in ref. [38].

To compute the homogenized macroscale response, affine displacement boundary conditions are applied to the boundary nodes of fibers and matrix of the RVE. Traction-free surfaces under the constraint of affine displacements at the boundary are approximated by leaving the normal displacement of a traction-free surface as a solution variable, which is then computed as part of the numerical solution in order to ensure energy minimization. From the reference position vectors \mathbf{X}^a of the boundary nodes and the corresponding nodal reaction forces \mathbf{f}^a calculated upon application of the boundary conditions, the homogenized first Piola–Kirchhoff stress tensor can be computed as [52]

$$\langle \mathbf{P} \rangle = \frac{1}{V_{\text{RVE}}} \sum_{a=1}^{N_b} \mathbf{f}^a \otimes \mathbf{X}^a, \quad (7)$$

where $V_{\text{RVE}} = s^3$ is the reference volume of the RVE and the sum is taken over all N_b boundary nodes. Swelling in response to a change in the external salt concentration was implemented by treating c_{ext} as a temperature-like field variable, which is accessed at the integration point level in the UMAT subroutine.

For simulation of indentation tests, the contact between a rigid, spherical indenter and the surface of the model domain is modeled as hard frictionless contact. Symmetry boundary conditions are imposed on the bottom surface as well as on the lateral surfaces of the domain. The force–displacement response is extracted from the imposed displacement and resulting reaction force on the reference point of the rigid body. Analogous to the data analysis of indentation experiments, the apparent elastic modulus is obtained from the simulation data by fitting the force–indentation curve to the Hertzian contact solution (Eq. (1)).

To compute the local stiffness within a 3D fiber network in a manner similar as probed by a dermal fibroblast, we model the contractile action of a polarized cell as a force dipole (cf. refs. [53,54]). The dipole is represented by the line segment connecting two fiber network crosslinks and is modeled as an axial connector element (CONN3D2) in Abaqus. We prescribe a 10% contraction of the dipole and extract the resulting force f ; the structural stiffness

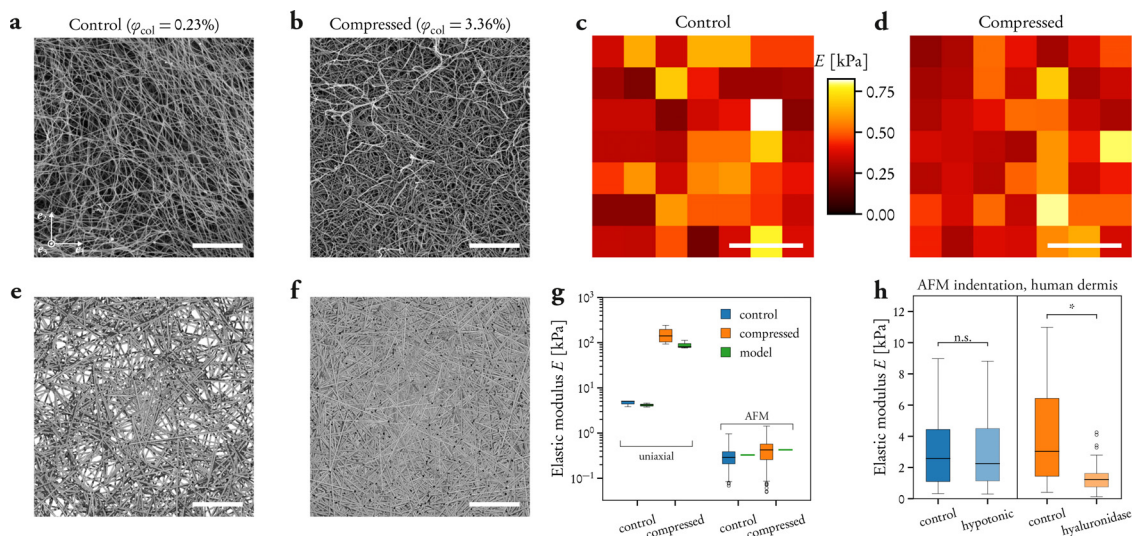


Fig. 3. Multiscale mechanical properties of dermal-equivalent collagen hydrogels. (a, b) Scanning electron micrographs of control (a) and plastically compressed (b) collagen hydrogels. Scale bars: 5 μm . (c, d) Surface distribution of AFM indentation measurements from representative control (c) and compressed (d) gels. The color bar applies to both images. Scale bars: 10 μm . (e, f) Top-view rendering of representative fiber network models of control (e) and compressed (f) gels. Scale bars: 5 μm . (g) UA tension ($n = 3, 9$) and AFM indentation ($n = 393, 435$) data and corresponding model predictions of the elastic modulus (3–5 simulations; green). (h, left) AFM indentation measurements on human dermis in PBS (control) and hypotonic (0.1 \times PBS) solution ($P = 0.7953, n = 64, 72$; Mann–Whitney U-test). (h, right) AFM indentation measurements on human dermis before (control) and after 60 min treatment with hyaluronidase ($P = 8 \times 10^{-6}, n = 48, 55$; Mann–Whitney U-test).

associated with this contraction is computed as $k = -f/u$, u being the axial displacement of the dipole.

2.7.6. Simulating the effect of surface topography

We consider a random surface $z = z(x, y)$ as a periodic function on a square domain of side length L , that is, $z : [0, L] \times [0, L] \rightarrow \mathbb{R}$. A spectral representation of the surface z is given by

$$z(x, y) = \sum_{i=-\infty}^{\infty} \sum_{j=-\infty}^{\infty} A_{ij} \cos(\mathbf{k}_{ij} \cdot \mathbf{x} + \phi_{ij}), \quad (8)$$

where A_{ij} and ϕ_{ij} are the amplitude and phase associated with the wave vector $\mathbf{k}_{ij} = \frac{2\pi}{L}(\mathbf{i}\mathbf{e}_1 + \mathbf{j}\mathbf{e}_2)$, respectively. To generate a random surface numerically, we sample the phase values from a uniform distribution, $\phi_{ij} \sim U(-\frac{\pi}{2}, \frac{\pi}{2})$, and the amplitude is computed according to $A_{ij} = g_{ij}/(i^2 + j^2)^{\gamma/2}$, with $A_{00} = 0$. Herein, g_{ij} is sampled from a normal distribution with zero mean and standard deviation σ (i.e., $g_{ij} \sim N(0, \sigma)$), and the spectral exponent γ describes the attenuation of higher frequencies. The infinite series is truncated symmetrically at $\pm N$, $N = \lceil L/\lambda_{\min} \rceil$, where λ_{\min} is the minimum wavelength considered. Random surfaces with topographical variations in line with AFM measurements (Fig. 2jk) were generated with $L = 40 \mu\text{m}$, $N = 80$, $\gamma = 1.5$, and $\sigma = 0.275 \mu\text{m}$ (Fig. 2l).

The random surfaces were imported into the finite element software Comsol Multiphysics® (version 5.4, COMSOL AB). Three-dimensional finite element models of the AFM indentation setup were created, and the domains were meshed with linear tetrahedral elements. The contact between the rigid, spherical indenter and the random surface was modeled as frictionless, and normal contact was implemented using the penalty method. To test whether the heterogeneous distribution of elastic moduli measured in AFM indentation experiments can be explained by surface topography rather than material heterogeneity, the material behavior was defined by the hyperelastic model for the ground matrix (Eq. (4)), that is, homogeneous. Indentation simulations were performed at 7×7 positions in a $30 \mu\text{m} \times 30 \mu\text{m}$ grid on this surface and analyzed analogously as the AFM experiments.

2.8. Data analysis

All data analysis was performed in Python (version 3.7.6, Python Software Foundation). Data are presented as mean \pm standard deviation, shown in standard boxplots, or visualized in form of the probability density function (Fig. 2o). Boxplots shown in logarithmic scale (e.g., Figs. 3g, 4h) were computed based on the log-transformed data. Where relevant, significant differences ($P < 0.05$, denoted by an asterisk) between two groups were analyzed using two-sided Student's t -test or Mann–Whitney U-test depending on the outcome of a Shapiro–Wilk test for normality. The P -values and sample sizes are reported in the respective figure legends.

3. Results

3.1. Mechanical properties of human skin across length scales

To illustrate the large variations in existing data on the elastic modulus of skin, we collected literature data from the last twenty years [16–18,20–23,40,55–57] and grouped them by animal species (human, mouse, pig) and testing technique used (indentation, *in vivo* suction, uniaxial (UA) tension), see Fig. 1a. (Further information is provided in Supplementary Note S1 and Table S1.) We focused on experiments assessing the mechanical behavior of the tissue at low strain rates, thus excluding dynamic measurements such as those based on shear wave elastography [58]. In line with previous observations [26], macroscopic tensile testing appears to yield much larger moduli than indentation-based testing (compare orange and blue bars in Fig. 1a), although large variations in the latter are apparent, both within and between studies. This points at general challenges related to indentation testing of highly deformable materials. In fact, when probing the mechanical properties of soft materials locally with a compliant sensing element, such as the cantilever of the AFM, proper testing conditions that eliminate spurious forces between the probe tip and the surface are essential. For example, we estimate that attractive forces due to surface tension under ambient conditions may be orders of magnitude larger than the elastic contact forces expected, thus biasing the results (see details in Supplementary Note S1.2).

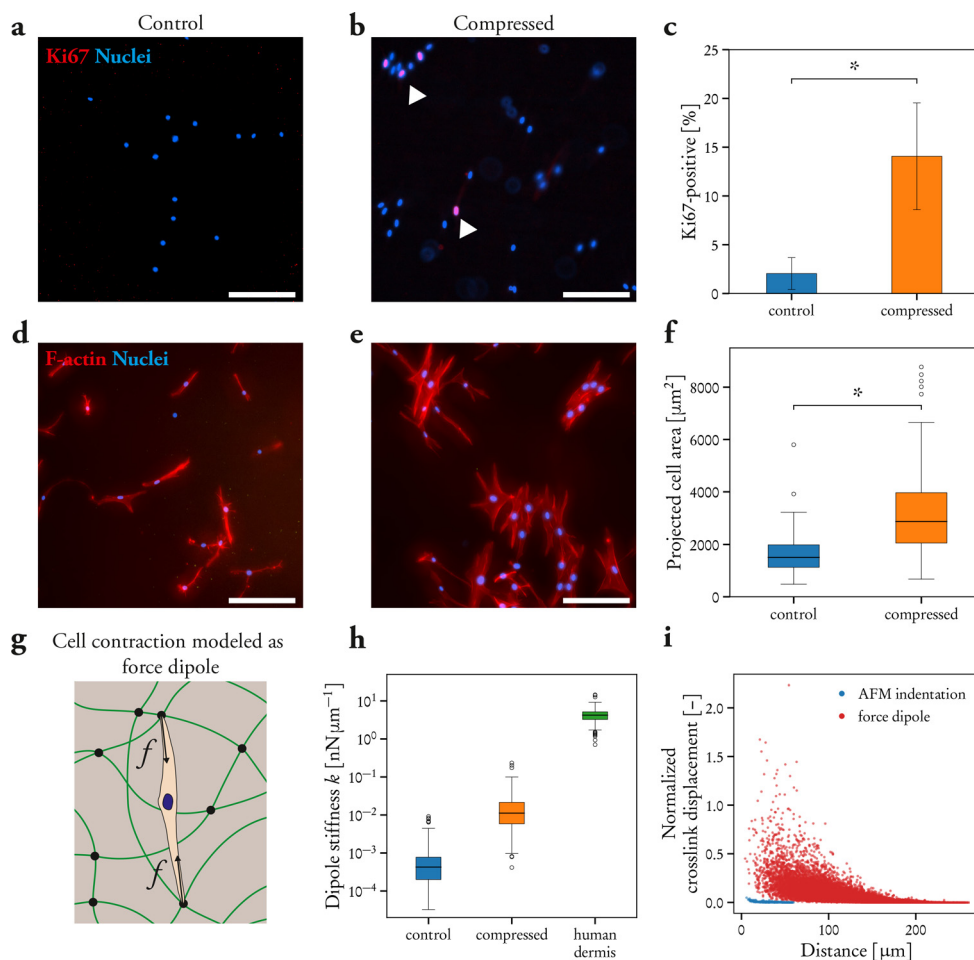


Fig. 4. Fibroblast mechanobiology in stiffness-tunable, dermal-equivalent collagen hydrogels. (a–c) Representative whole-mount immunofluorescence micrographs of human dermal fibroblasts embedded in collagen gels and stained for the proliferation marker Ki67 (a, b), showing the higher cell proliferation rate in compressed gels (c; $P = 0.0409$, $n = 3$, Student's t -test). White arrowheads highlight Ki67-positive nuclei in the compressed gel (b). (d–f) Representative whole-mount F-actin immunostainings (d, e) demonstrate larger cell size in stiffer, plastically compressed gels (f; $P = 1.8 \times 10^{-22}$, $n_{\text{cells}} = 128, 159$ from three independent experiments, Mann–Whitney U-test). Scale bars (a, b, d, e): 200 μm . (g) Analysis of microscale tissue mechanics as perceived by a polarized cell *in vivo* by modeling cell contraction as a force dipole. (h) Simulation of the dipole stiffness resulting from a 10% cell contraction in control and compressed collagen hydrogels compared to the human dermis *in vivo* ($n = 300, 167, 182$ dipoles from 3–5 random networks). (i) Displacement magnitude at fiber crosslinks under AFM indentation and force dipole contraction as a function of distance from the contact point and the dipole center, respectively. The displacement data are normalized by the AFM indentation depth and half the axial displacement of the dipole, respectively.

Next, we analyzed whether differences in testing conditions as well as inherent biological variations between donors could explain the large differences in moduli measured. To this end, we tested the mechanical properties of human dermis (Fig. 1b) using different techniques (see Section 2.5): uniaxial and equibiaxial tension, microindentation (indenter radius $R = 100 \mu\text{m}$), and AFM indentation ($R = 3.05 \mu\text{m}$) (Fig. 1cde). All experiments were performed with the tissue immersed in physiological buffer solution. Tensile tests were performed at low strain rates to characterize the elastic long-term equilibrium behavior of the tissue [16], whereas indentation experiments used a displacement rate leading to small Péclet numbers [38]. Thus, fluid flow is much faster than the deformation rates applied, and the measurements correspond to the long-term response of the tissue. From UA tension tests, we calculate the elastic modulus as the initial slope of the nominal stress–stretch (P – λ_1) curve (Fig. 1c). For comparison, note that the tangent moduli extracted at higher stresses can be orders of magnitude larger due to the strong strain-stiffening behavior (cf. Fig. 1ac), which is particularly prominent in biaxial tension (Fig. 1c). From the indentation data, we determine an apparent elastic modulus by fitting each force–indentation curve to the Hertzian solution for the contact between a rigid, spherical inden-

ter and a flat, elastic half-space (Section 2.5.1). Remarkably, only minor differences between donors were detected with all three measurement techniques (Fig. 1fgh). In particular, the variability between donors is not larger than that observed for each donor individually. The scatter observed in the tensile modulus (Fig. 1f) is related to the variability in collagen and interstitial fluid content of each test piece, as reported previously for other soft tissues (e.g., refs. [59,60]). The intradonor variability in indentation experiments (Fig. 1gh) is more significantly affected by surface topography, as shown in Section 3.2. Importantly, the data in Fig. 1fgh reproduce the difference in modulus by several orders of magnitude between microscale indentation and macroscale tension (cf. Fig. 1a). Indeed, whereas the elastic modulus measured in macroscale UA tension is on the order of 100 kPa to 200 kPa, the modulus measured by both micro- and AFM indentation is two orders of magnitude lower (compare Fig. 1f with gh). Furthermore, despite the difference in microstructure between the papillary and the reticular dermis (Fig. 1b), the stiffness of these layers is similar when measured by AFM (Fig. 1h). Additionally, in agreement with previous works [20,21,55], the AFM data for each donor contain large variations itself, from 0.1 to 10 kPa. Similar results were obtained when repeating the experiments on wild-type mouse skin, both in terms

of a two orders of magnitude difference between the moduli measured in UA tension versus AFM indentation as well as the large scatter in the moduli measured at the microscale by AFM (Supplementary Fig. S8). We also validated our testing protocols on samples of a soft PDMS elastomer (Supplementary Fig. S7), confirming that identical E are measurable with all testing techniques for a material that may be regarded as a homogeneous continuum at all length scales considered. These results demonstrate that neither testing errors nor biological variations can account for the discrepancies in moduli observed, and we therefore hypothesized that they might originate from the composition and structure of the materials considered.

3.2. A fiber network model of the human dermis can rationalize measurements across scales

The human dermis, composed primarily of collagen fibers (volume fraction $\varphi_{\text{col}} \sim 22\%$), interstitial fluid ($\sim 70\%$), elastin ($\sim 1.2\%$), and proteoglycans ($< 1\%$), is the load-bearing layer of the skin [3]. A simplistic explanation for the large range of moduli observed (Fig. 1a) may be derived from a rule-of-mixture analysis. Given a tensile modulus of collagen fibers $E_{\text{col}} \sim 100$ MPa to 360 MPa [61] and a matrix modulus $E_{\text{m}} \sim \text{kPa}$, we obtain the (approximate) upper (Voigt) and lower (Reuss) bounds on the composite modulus,

$$E_{\text{m}}/(1 - \varphi_{\text{col}}) < E < \varphi_{\text{col}}E_{\text{col}}, \quad (9)$$

which covers a range from kPa to 20 MPa to 80 MPa. Although the upper bound may be considered a good approximation of the tensile stiffness at high strains when fibers are aligned along the loading direction [62] (cf. Fig. 1ac), the geometrical and topological arrangement of fibers and matrix that corresponds to these bounds is clearly not representative of skin *in vivo*. The rule-of-mixture bounds therefore provide little information about, for example, the *in vivo* tissue stiffness and the deformation mechanisms at the microscale.

To answer such questions and rationalize the experimental results, we modeled the dermis as a composite consisting of a discrete, random network of collagen fibers embedded in a ground matrix (Fig. 2a; see Section 2.7 for details). This ground matrix is composed of interstitial fluid, elastin, and proteoglycans (Fig. 2a), and we modeled it as a continuum at the length scales considered. In contrast, the collagen fiber network is characterized by intrinsic length scales, such as the density of fiber crosslinks, the fiber segment length, and the cross-sectional dimensions of the fibers. Using data on the dermis composition and its collagen network topology (Section 2.7.4), we generated fiber networks (Fig. 2c) in which fiber segments are modeled as slender, elastic springs with low resistance to compression and with high stiffness in tension (Fig. 2b). Next, constitutive model parameters for fibers and ground matrix were selected to reproduce UA stress–stretch and 3D kinematics data of human skin (Fig. 2de; ref. [16]). The progressive rotation of fibers toward the loading direction explains both the well-known strain-stiffening behavior (Fig. 2d) and the large lateral contractions (Fig. 2e); see also Supplementary Fig. S11. To validate the model on the macroscale, we performed membrane inflation experiments (see Section 2.5.4) to characterize the equibiaxial stress–stretch response (P – λ_{eb}) of human skin (Fig. 2f) and analyzed existing biaxial *in vivo* data (Fig. 2g; refs. [39,40], see Supplementary Note S2). The model provides a reasonable prediction of both datasets (Fig. 2fg), including the stiffness at stress states representative of *in vivo* conditions (Fig. 2g).

We then used the model to analyze the tissue behavior when tested in indentation with the AFM. Here, the model predicts an apparent stiffness that is determined solely by the matrix properties, independent of the local fiber network orientation (Fig. 2h)

and the matrix–network coupling (Supplementary Fig. S12e). To understand this result, we calculated the intersection of all fibers with the indentation surface (Supplementary Fig. S9), showing that the phase most likely probed with the AFM is indeed the ground matrix ($\sim 82\%$ of the surface area for the reference network). We then asked whether probing the dermis with a larger indenter would be able to activate the fiber network when a larger subset of fibers is directly within the contact area. This intuitive explanation holds, however, only if the matrix and network are entangled at the microscale and loads can be transferred between the phases (Supplementary Fig. S12f). In contrast, when the matrix–network entanglement is weak, the indentation modulus is close to the modulus of the ground matrix also for the larger indenter, suggesting that the network is able to rearrange to another zero-energy state despite the applied load. Note that this length-scale independence is in fact also observed when comparing the AFM and microindentation measurements (Fig. 1gh), indicating that the corresponding entanglement between the ground matrix and the fiber network in the dermis is weak. To illustrate the underlying deformation mechanism, we compared the distribution of fiber strains under a tensile stress representative of the *in vivo* state ($P = 5$ kPa) with the fiber strains experienced under AFM and microindentation (Fig. 2i). Grouping fibers as ‘undeformed’ ($|\varepsilon| < 1 \times 10^{-5}$), compressed ($\varepsilon < -1 \times 10^{-5}$), straightening ($1 \times 10^{-5} < \varepsilon < \varepsilon_s$), or in tension ($\varepsilon > \varepsilon_s$) (cf. Fig. 2b) demonstrates that a fiber network under macroscale tension includes both compressed as well as stretched, load-bearing fibers. In contrast, fibers in a network under indentation remain essentially undeformed, with no load-bearing fibers and only a larger number of compressed fibers for larger indenter radii.

Although our model explains the difference in stiffness between macroscale tension and microscale indentation data by two distinct deformation mechanisms of the fiber network, the majority of the moduli measured by AFM and microindentation (~ 1 kPa to 2 kPa) is lower than that predicted by the model (~ 4 kPa). In principle, this prediction could be improved by decreasing the shear modulus of the matrix (Supplementary Fig. S12a), which, however, would compromise the representation of the kinematics in UA tension (Fig. 2e). In addition, our model does not offer an explanation for the large variation in AFM indentation moduli measured (Fig. 1h). These observations led us to hypothesize that the heterogeneity observed is not necessarily due to local differences in material behavior, but a pure geometrical effect arising due to surface roughness, which also reduces the contact area compared to indentations on a flat surface.

To test this hypothesis, we first measured the topography of hydrated dermal cryosections using contact mode AFM imaging (Fig. 2jk). Next, we defined a spectral representation of random surfaces with topographical variations (see Section 2.7.6), which can be parametrized to generate surfaces similar to those measured (Fig. 2l). Using the material model of the ground matrix (equivalent elastic modulus $E_{\text{m}} = 4.14$ kPa; dotted line in Fig. 2h), we replicated the AFM indentation protocol *in silico* by finite element simulations, and the simulation data were analyzed analogously as the experiments; that is, assuming Hertzian contact with a flat surface. The surface distribution of moduli obtained shows an apparent heterogeneity (Fig. 2m), qualitatively similar to the AFM experiments (Fig. 2n). Moreover, comparing the probability distribution of simulation data from multiple random surfaces with the entire AFM dataset shows a striking agreement (Fig. 2o). In addition, we note that the shape of the distribution of the AFM modulus for human skin is similar to that measured for both murine papillary and reticular dermis (Supplementary Fig. S8c) as well as that measured previously for human dermis [20]. These results demonstrate that a major part of the variation in AFM data can be explained by surface roughness independent of local material

heterogeneity. Moreover, the simulations show that the presence of surface roughness shifts the apparent modulus distribution to lower values than the actual material stiffness (cf. Fig. 2h), which is expected since the true contact area with a rough surface is smaller than the one estimated for a perfectly flat surface.

We further asked whether the effect of topography might be diminishing at the length scale of the microindentation experiments. This would be expected if there is separation of scales between the length scale of indentation and the surface roughness. To this end, we measured the topography of dermal cross-sections used for microindentation tests by laser-scanning confocal microscopy (Supplementary Fig. S14). However, the root-mean-square roughness $S_q = 12.39 \pm 3.37 \mu\text{m}$ measured is in fact comparable to the indentation depth ($\sim 10 \mu\text{m}$). This demonstrates that also the microindentation data (Fig. 1g) are influenced by surface topography, and explains why the moduli measured are indeed lower than those predicted by the model (Supplementary Fig. S12f).

3.3. Indentation testing does not activate the collagen fiber network

Based on the experiments and corresponding computational analyses (Figs. 1–2), we therefore hypothesized that indentation testing cannot be used to activate the load-bearing mechanism of the collagen fiber network in the dermis. To challenge this hypothesis, we first made use of dermal-equivalent collagen hydrogels as a simple model system for which the volume fraction of collagen fibers is tunable toward that of the native tissue ($\varphi_{\text{col}} \sim 22\%$) by plastic compression [63]. We measured the elastic modulus of control gels ($\varphi_{\text{col}} = 0.23\%$; Fig. 3a) and denser gels that underwent plastic compression ($\varphi_{\text{col}} = 3.36\%$; Fig. 3b) in AFM indentation (Fig. 3cd), microindentation ($R = 500 \mu\text{m}$, see Supplementary Fig. S15), and in UA tension. To corroborate the experiments, we developed fiber network models of the two materials based on their composition and network topology as well as simulations of the plastic compression process (Fig. 3ef; see Section 2.7.4 for details). As expected, macroscale tension experiments clearly distinguish the difference between the two materials (Fig. 3g). Conversely, both AFM (Fig. 3g) and microindentation (Supplementary Fig. S15a) measurements show that the indentation modulus of the two materials is similar, despite the almost 15-fold difference in collagen concentration. Note also the large difference between tensile and indentation moduli for both materials, which is in line with the human skin data (Fig. 1). The fiber network model predicts both the concentration-dependent tensile stiffness as well as the concentration-independent indentation stiffness (Fig. 3g), confirming the hypothesis that indentation does not engage the fiber network.

To test the hypothesis for the case of human dermis, we exposed the dermis to a hypotonic solution ($0.1 \times \text{PBS}$), which causes tissue swelling and thus leads to a state of extension in the collagen fibers [16]. If the fibers were bearing load under AFM indentation, the swollen tissue would be perceived stiffer because of the strain-stiffening behavior of the fibers (cf. Fig. 2b). In contrast, we observe a stiffness that is independent of the state of swelling (Fig. 3h, left), in line with our hypothesis. Moreover, our simulations have indicated that the ground matrix is the primary determinant of the tissue indentation stiffness (Fig. 2g). To directly assess this conclusion, we treated dermal sections for AFM indentation with hyaluronidase in order to reduce the content of hyaluronic acid, which, despite being a minor tissue component, contributes to tissue hydration and the gel-like state of the ground matrix [64]. Interestingly, digestion of hyaluronic acid causes a significant decrease in the AFM stiffness measured (Fig. 3h, right), again aligned with our model predictions.

3.4. Implications for dermal cell mechanobiology

Indentation measurements offer the possibility to probe the tissue at the length scale of cells ($\sim 10 \mu\text{m}$ to $100 \mu\text{m}$) and subcellular structures such as focal adhesions ($\sim 1 \mu\text{m}$) [20]. However, our experiments and model predictions indicate that, for skin and collagen hydrogels, indentation does not deform the collagen fiber network, which is the tissue structure dermal cells attach to and activate through focal adhesions to probe their environment. Intriguingly, similar results have recently been reported for synthetic fibrous hydrogels [65]. These results question the use of indentation measurements to infer the stiffness perceived by dermal cells.

To test this conclusion experimentally, we embedded primary human dermal fibroblasts in control and plastically compressed collagen gels and analyzed two established markers of stiffness-dependent cell response in 2D culture: proliferation [66,67] and cell spreading [68,69]. In line with previous 2D studies, we observe by whole-mount immunofluorescence microscopy that fibroblasts in the stiffer, plastically compressed gels are more proliferative (Fig. 4a–c) and spread to larger area (Fig. 4d–f) than cells in the softer control gels. These results could not have been predicted solely based on AFM data. Instead, to estimate the stiffness sensed by a resident cell in three-dimensional fibrous networks, we model the contractile action of a polarized cell as a force dipole acting on fiber crosslinks (Fig. 4g). In contrast to the AFM results (Fig. 3cdg), the force dipole simulations predict that the collagen concentration strongly influences the cell traction forces, suggesting that dermal cells would be able to distinguish between the two materials as well as between the comparatively low-concentration hydrogels and the native dermis (Fig. 4h). To illustrate the underlying deformation mechanisms of the fiber network that explain the difference between cell contraction and AFM indentation, we compare the displacement fields in the vicinity of the dipole and the contact point, respectively (Fig. 4i). Here, force dipole simulations result in a long-ranged fiber engagement and crosslink displacement decay (Fig. 4i, red dots), which has been observed in collagen gel tissue models [9]. Noteworthy, this state of deformation cannot be reproduced by indentation (Fig. 4i, blue dots).

4. Discussion

The elastic modulus is a concept of continuum mechanics whose application to soft biological tissues is not straightforward. Its definition as the initial slope of the uniaxial stress–strain curve implies the definition of a reference configuration, which does not exist a priori. At least, a unique definition is lacking both *in vivo* (due to the physiological residual tension) and *in ex vivo* testing (because of the lack of a clear transition between sample straightening and stretching, see Supplementary Note S1.1). An extended definition of the elastic modulus as the slope at a given level of stress (i.e., the tangent modulus) requires additional information about the specific loading conditions and the stress and strain measures used. Although the term ‘elastic’ indicates that the deformation is assumed fully reversible upon unloading, the concept is frequently used independent of the nature of the material behavior, as soft tissue properties generally depend on both time and loading history. For human and murine skin, poro- and viscoelasticity play a particular role in this regard as indicated in our recent study [16], and we have designed the here-presented experiments to keep their influence on the results at a low level. Perhaps most critical, the modulus as a continuum-mechanical quantity implies that the tissue can be regarded as a homogenized material at the length scales considered. In particular, when soft connective tissue properties are analyzed at a length scale comparable to the geometrical features of the collagen fiber network, such as in the case of AFM indentation, this continuum hypothesis becomes invalid.

These limitations are affecting the essential task of characterizing the rigidity of soft biological tissues at macroscopic and cellular length scales, which is important for manifold biomedical applications [12–14,20]. It is therefore both useful and admissible to describe the stiffness perceived at different length scales and under different loading conditions in terms of ‘apparent’ elastic moduli, leading to the large discrepancies in the values reported (Fig. 1a).

Here, we addressed these discrepancies by analyzing the underlying physics governing human skin mechanics from tissue down to cellular length scales. Based on a multiscale model of the human dermis, we explain the macroscale stiffness *in vivo* and at physiological and suprphysiological stresses as a result of the activation of the collagen fiber network: under an applied tensile stress, fibers rotate toward the loading direction and contribute to bearing the load [62]. This strain-stiffening behavior (Fig. 1c) is accompanied by large lateral contractions (Fig. 2e) and volume loss [16]. In contrast, when the tissue is indented or, more generally, compressed (Supplementary Fig. S11), the combination of the weak load-bearing capability of fibers under compression (Supplementary Results and Discussion S5.4) and the weak entanglement with the surrounding ground matrix (Supplementary Fig. S12) allows the fiber network to rearrange and avoid bearing load. We confirmed this interpretation both experimentally and computationally using a stiffness-tunable model system based on plastically compressed, dermal-equivalent collagen hydrogels (Fig. 3).

Although our model representation is a clear simplification compared to the actual microstructure of the human dermis, it is able to predict the mechanical behavior of skin under various states of deformation at both the macro- and the microscale (Fig. 2) as well as under more complex boundary conditions that include altering the osmolarity of the external bath (Supplementary Fig. S13). Noteworthy, this is achieved despite a simple model representation of collagen fiber segments as nonlinear, one-dimensional springs. These aspects may explain the small subset (~ 11.1%) of AFM data for which the apparent modulus is larger than that of the matrix and thus cannot be explained by surface topography (Fig. 2o). Note, however, that these ‘stiff’ AFM data points (~ 5 kPa to 10 kPa) are orders of magnitude softer than the tensile modulus of collagen fibers (~ 100 MPa to 360 MPa, [61]). In fact, we are able to recover this subset of AFM data by simulating indentations directly on top of fiber network nodes (Supplementary Fig. S9c). Noteworthy, even in the case of direct indentation on a fiber cross-section, long-range displacement decay like that observed due to cell contraction (Fig. 4i) is still not activated since the fiber network is loaded in compression rather than tension (Supplementary Results and Discussion S5.2).

The ground matrix also plays an important role in the mechanics of soft connective tissues by supporting compressive loads and stabilizing the material behavior in lateral directions under tensile loading (Supplementary Results and Discussion S5.4). Here, we describe the distortional and dilatational behavior of the ground matrix with a simple, phenomenological continuum model. While the water-retaining osmotic effect resulting from ion imbalance due to charged glycosaminoglycan chains attached to the proteoglycan core proteins is accounted for explicitly, the physicochemical origin of the distortional stiffness of the ground matrix is less obvious. In the dermis, the existence of a hydrated, gel-like network of crosslinked hyaluronic acid and proteoglycans, entrapped within the collagen meshwork, motivates a resistance to changes in shape [64]. This is confirmed by indentation experiments following enzymatic digestion of hyaluronidase (Fig. 3h). Moreover, other solid constituents (e.g., elastin, fibronectin) are also likely to contribute to the shear stiffness of the ground matrix. We expect such fibrous components to be primarily in a stretched state within the tissue so that the difference between their tensile and compressive response does not affect the mechanical behavior of the ground

matrix. Noteworthy, all such constituents are lacking in collagen gels. This is particularly fascinating since the matrix shear modulus is the most influential parameter determining the indentation modulus (Supplementary Fig. S10), which therefore is key to predicting the AFM and microindentation experiments (Supplementary Fig. S15c). In collagen hydrogels, the low but non-negligible shear stiffness of the matrix may arise from an ordered structure of water molecules associated with the hydrophilic polymers; it has been proposed that these water molecules are restricted in their motion and cannot displace or rotate independently of their neighbors [70].

The ECM stiffness perceived by dermal cells is a quantity of primary interest for applications in skin mechanobiology and tissue engineering [12,20]. Whereas the cell-relevant ECM stiffness has commonly been interpreted as the modulus measured using AFM indentation at the length scale of cells [20,28–30], we have demonstrated that such measurements do not necessarily represent the ECM stiffness perceived by resident cells, as the corresponding deformation mechanisms are distinct. In fact, cell behavior in stiffness-tunable, dermal-equivalent collagen hydrogels does not correlate with the results of indentation measurements (Figs. 3–4). The strongly loadcase-dependent mechanical behavior of connective tissues (Fig. 3g), which originates in the tension–compression nonlinearity of rope-like fiber segments, is in stark contrast with that of common homogeneous material model systems in mechanobiology (e.g., PDMS elastomers and polyacrylamide hydrogels [71]). Alternative techniques, for example based on optical or magnetic manipulation of micrometer-sized beads or rods embedded within the ECM [72–74] and corroborated by appropriate models of the microstructure, may therefore be more suitable to assess ECM stiffness as perceived by single cells. We expect the present results to apply to a wide range of native and reconstituted soft connective tissues with similar composition and microstructure (cf. ref. [26]).

Data availability

The raw/processed data required to reproduce these findings are available upon request.

Declaration of Competing Interest

The authors declare that they have no known competing financial interests or personal relationships that could have appeared to influence the work reported in this paper.

CRediT authorship contribution statement

Adam Wahlsten: Conceptualization, Methodology, Software, Validation, Formal analysis, Investigation, Data curation, Visualization, Writing – original draft, Writing – review & editing. **Alberto Stracuzzi:** Methodology, Writing – review & editing. **Ines Luchtefeld:** Methodology, Investigation. **Gaetana Restivo:** Resources, Data curation. **Nicole Lindenblatt:** Resources. **Costanza Giampietro:** Methodology, Investigation. **Alexander E. Ehret:** Conceptualization, Methodology, Writing – review & editing. **Edoardo Mazza:** Conceptualization, Methodology, Validation, Resources, Writing – review & editing, Supervision, Project administration, Funding acquisition.

Acknowledgments

This work was conducted as part of the research initiative [Skintegrity.ch](https://www.skintegrity.ch) and supported financially by the Swiss National Science Foundation (grants no. 179012 and CRSII5_213498 to E.M.). The numerical simulations were performed on the Euler HPC cluster operated by the High Performance Computing group at

ETH Zurich. We gratefully acknowledge Dr. Mateusz Wietecha and Dr. Andrii Kuklin (Institute for Molecular Health Sciences, ETH Zurich) for providing murine skins, the Tissue Biology Research Unit (University Children's Hospital Zurich), in particular Dr. Dominic Rüttsche, for providing primary human dermal fibroblasts and for use of the cryotome, Dr. Marco Pensalfini (Institute for Mechanical Systems, ETH Zurich) for the scanning electron micrographs of the collagen hydrogels, and the lab of Prof. Mirko Meboldt (Product Development Group, ETH Zurich) for use of the confocal laser scanning microscope for surface characterization.

Supplementary material

Supplementary material associated with this article can be found, in the online version, at doi:[10.1016/j.actbio.2023.08.030](https://doi.org/10.1016/j.actbio.2023.08.030).

References

- [1] A. Dance, The secret forces that squeeze and pull life into shape, *Nature* 589 (7841) (2021) 186–188, doi:[10.1038/d41586-021-00018-x](https://doi.org/10.1038/d41586-021-00018-x).
- [2] W. Yang, V.R. Sherman, B. Gludovatz, E. Schaible, P. Stewart, R.O. Ritchie, M.A. Meyers, On the tear resistance of skin, *Nat. Commun.* 6 (2015) 1–10, doi:[10.1038/ncomms7649](https://doi.org/10.1038/ncomms7649).
- [3] G. Limbert, Mathematical and computational modelling of skin biophysics: a review, *Proc. R. Soc. A Math. Phys. Eng. Sci.* 473 (2017) 20170257, doi:[10.1098/rspa.2017.0257](https://doi.org/10.1098/rspa.2017.0257).
- [4] J.D. Humphrey, E.R. Dufresne, M.A. Schwartz, Mechanotransduction and extracellular matrix homeostasis, *Nat. Rev. Mol. Cell Biol.* 15 (12) (2014) 802–812, doi:[10.1038/nrm3896](https://doi.org/10.1038/nrm3896).
- [5] D.E. Discher, P.A. Janmey, Y.I. Wang, Tissue cells feel and respond to the stiffness of their substrate, *Science* 310 (5751) (2005) 1139–1143, doi:[10.1126/science.1116995](https://doi.org/10.1126/science.1116995).
- [6] M. Aragona, A. Sifrim, M. Malfait, Y. Song, J. Van Herck, S. Dekoninck, S. Gargouri, G. Lapouge, B. Swedlund, C. Dubois, P. Baatsen, K. Vints, S. Han, F. Tissir, T. Voet, B.D. Simons, C. Blanpain, Mechanisms of stretch-mediated skin expansion at single-cell resolution, *Nature* 584 (7820) (2020) 268–273, doi:[10.1038/s41586-020-2555-7](https://doi.org/10.1038/s41586-020-2555-7).
- [7] B. Hinz, D. Mastrangelo, C.E. Iselin, C. Chaponnier, G. Gabbiani, Mechanical tension controls granulation tissue contractile activity and myofibroblast differentiation, *Am. J. Pathol.* 159 (3) (2001) 1009–1020, doi:[10.1016/S0002-9440\(10\)61776-2](https://doi.org/10.1016/S0002-9440(10)61776-2).
- [8] A. Wahlsten, D. Rüttsche, M. Nanni, C. Giampietro, T. Biedermann, E. Reichmann, E. Mazza, Mechanical stimulation induces rapid fibroblast proliferation and accelerates the early maturation of human skin substitutes, *Biomaterials* 273 (2021) 120779, doi:[10.1016/j.biomaterials.2021.120779](https://doi.org/10.1016/j.biomaterials.2021.120779).
- [9] P. Pakshir, M. Alizadehgiashi, B. Wong, N.M. Coelho, X. Chen, Z. Gong, V.B. Shenoy, C. McCulloch, B. Hinz, Dynamic fibroblast contractions attract remote macrophages in fibrillar collagen matrix, *Nat. Commun.* 10 (1) (2019) 1–17, doi:[10.1038/s41467-019-09709-6](https://doi.org/10.1038/s41467-019-09709-6).
- [10] E. Hadjipanayi, V. Mudera, R.A. Brown, Close dependence of fibroblast proliferation on collagen scaffold matrix stiffness, *J. Tissue Eng. Regen. Med.* 3 (2) (2009) 77–84, doi:[10.1002/term.136](https://doi.org/10.1002/term.136).
- [11] V.W. Wong, S. Akaishi, M.T. Longaker, G.C. Gurtner, Pushing back: wound mechanotransduction in repair and regeneration, *J. Invest. Dermatol.* 131 (11) (2011) 2186–2196, doi:[10.1038/jid.2011.212](https://doi.org/10.1038/jid.2011.212).
- [12] C.F. Guimarães, L. Gasperini, A.P. Marques, R.L. Reis, The stiffness of living tissues and its implications for tissue engineering, *Nat. Rev. Mater.* 5 (2020) 351–370, doi:[10.1038/s41578-019-0169-1](https://doi.org/10.1038/s41578-019-0169-1).
- [13] D.-H. Kim, N. Lu, R. Ma, Y.-S. Kim, R.-H. Kim, S. Wang, J. Wu, S.M. Won, H. Tao, A. Islam, K.J. Yu, T.-i. Kim, R. Chowdhury, M. Ying, L. Xu, M. Li, H.-J. Chung, H. Keum, M. McCormick, P. Liu, Y.-W. Zhang, F.G. Omenetto, Y. Huang, T. Coleman, J.A. Rogers, Epidermal electronics, *Science* 333 (6044) (2011) 838–843, doi:[10.1126/science.1206157](https://doi.org/10.1126/science.1206157).
- [14] T. Lee, E.E. Vaca, J.K. Ledwon, H. Bae, J.M. Topczewska, S.Y. Turin, E. Kuhl, A.K. Gosain, A.B. Tepole, Improving tissue expansion protocols through computational modeling, *J. Mech. Behav. Biomed. Mater.* 82 (2018) 224–234, doi:[10.1016/j.jmbbm.2018.03.034](https://doi.org/10.1016/j.jmbbm.2018.03.034).
- [15] J.M. Phillip, I. Aifuwa, J. Walston, D. Wirtz, The mechanobiology of aging, *Annu. Rev. Biomed. Eng.* 17 (1) (2015) 113–141, doi:[10.1146/annurev-bioeng-071114-040829](https://doi.org/10.1146/annurev-bioeng-071114-040829).
- [16] A. Wahlsten, M. Pensalfini, A. Stracuzzi, G. Restivo, R. Hopf, E. Mazza, On the compressibility and poroelasticity of human and murine skin, *Biomech. Model. Mechanobiol.* 18 (4) (2019) 1079–1093, doi:[10.1007/s10237-019-01129-1](https://doi.org/10.1007/s10237-019-01129-1).
- [17] A.N. Annaidh, K. Bruyère, M. Destrade, M.D. Gilchrist, M. Otténio, Characterization of the anisotropic mechanical properties of excised human skin, *J. Mech. Behav. Biomed. Mater.* 5 (1) (2012) 139–148, doi:[10.1016/j.jmbbm.2011.08.016](https://doi.org/10.1016/j.jmbbm.2011.08.016).
- [18] A. Pissarenko, W. Yang, H. Quan, K.A. Brown, A. Williams, W.G. Proud, M.A. Meyers, Tensile behavior and structural characterization of pig dermis, *Acta Biomater.* 86 (2019) 77–95, doi:[10.1016/j.actbio.2019.01.023](https://doi.org/10.1016/j.actbio.2019.01.023).
- [19] R. Oftadeh, B.K. Connizzo, H.T. Nia, C. Ortiz, A.J. Grodzinsky, Biological connective tissues exhibit viscoelastic and poroelastic behavior at different frequency regimes: application to tendon and skin biophysics, *Acta Biomater.* 70 (2018) 249–259, doi:[10.1016/j.actbio.2018.01.041](https://doi.org/10.1016/j.actbio.2018.01.041).
- [20] V.F. Achterberg, L. Buscemi, H. Diekmann, J. Smith-Clerc, H. Schwengler, J.J. Meister, H. Wenck, S. Gallinat, B. Hinz, The nano-scale mechanical properties of the extracellular matrix regulate dermal fibroblast function, *J. Invest. Dermatol.* 134 (7) (2014) 1862–1872, doi:[10.1038/jid.2014.90](https://doi.org/10.1038/jid.2014.90).
- [21] R.J. Petrie, N. Gavara, R.S. Chadwick, K.M. Yamada, Nonpolarized signaling reveals two distinct modes of 3D cell migration, *J. Cell Biol.* 197 (3) (2012) 439–455, doi:[10.1083/jcb.201201124](https://doi.org/10.1083/jcb.201201124).
- [22] M.L. Crichton, B.C. Donose, X. Chen, A.P. Raphael, H. Huang, M.A. Kendall, The viscoelastic, hyperelastic and scale dependent behaviour of freshly excised individual skin layers, *Biomaterials* 32 (20) (2011) 4670–4681, doi:[10.1016/j.biomaterials.2011.03.012](https://doi.org/10.1016/j.biomaterials.2011.03.012).
- [23] C. Dagdeviren, Y. Shi, P. Joe, R. Ghaffari, G. Balooch, K. Usugaonkar, O. Gur, P.L. Tran, J.R. Crosby, M. Meyer, Y. Su, R. Chad Webb, A.S. Tedesco, M.J. Slepian, Y. Huang, J.A. Rogers, Conformal piezoelectric systems for clinical and experimental characterization of soft tissue biomechanics, *Nat. Mater.* 14 (7) (2015) 728–736, doi:[10.1038/nmat4289](https://doi.org/10.1038/nmat4289).
- [24] L.R.G. Treloar, Stress-strain data for vulcanised rubber under various types of deformation, *Trans. Faraday Soc.* 40 (1944) 59, doi:[10.1039/tf9444000059](https://doi.org/10.1039/tf9444000059).
- [25] J.E. Field, The mechanical and strength properties of diamond, *Rep. Prog. Phys.* 75 (12) (2012) 126505, doi:[10.1088/0034-4885/75/12/126505](https://doi.org/10.1088/0034-4885/75/12/126505).
- [26] C.T. McKee, J.A. Last, P. Russell, C.J. Murphy, Indentation versus tensile measurements of Young's modulus for soft biological tissues, *Tissue Eng. Part B Rev.* 17 (3) (2011) 155–164, doi:[10.1089/ten.teb.2010.0520](https://doi.org/10.1089/ten.teb.2010.0520).
- [27] H.K. Graham, J.C. McConnell, G. Lambert, M.J. Sherratt, How stiff is skin? *Exp. Dermatol.* 28 (2019) 4–9, doi:[10.1111/exd.13826](https://doi.org/10.1111/exd.13826).
- [28] A.J. Engler, F. Rehfeldt, S. Sen, D.E. Discher, Microtissue elasticity: measurements by atomic force microscopy and its influence on cell differentiation, *Methods Cell Biol.* 83 (07) (2007) 521–545, doi:[10.1016/S0091-679X\(07\)83022-6](https://doi.org/10.1016/S0091-679X(07)83022-6).
- [29] S.R. Caliari, J.A. Burdick, A practical guide to hydrogels for cell culture, *Nat. Methods* 13 (5) (2016) 405–414, doi:[10.1038/nmeth.3839](https://doi.org/10.1038/nmeth.3839).
- [30] M.D.A. Norman, S.A. Ferreira, G.M. Jowett, L. Zozec, E. Gentleman, Measuring the elastic modulus of soft culture surfaces and three-dimensional hydrogels using atomic force microscopy, *Nat. Protoc.* 16 (2021) 2418–2449, doi:[10.1038/s41596-021-00495-4](https://doi.org/10.1038/s41596-021-00495-4).
- [31] R. Hopf, L. Bernardi, J. Menze, M. Zündel, E. Mazza, A. Ehret, Experimental and theoretical analyses of the age-dependent large-strain behavior of Sylgard 184 (10:1) silicone elastomer, *J. Mech. Behav. Biomed. Mater.* 60 (2016) 425–437, doi:[10.1016/j.jmbbm.2016.02.022](https://doi.org/10.1016/j.jmbbm.2016.02.022).
- [32] A.M. Reyes Lua, R. Hopf, E. Mazza, Factors influencing the mechanical properties of soft elastomer substrates for traction force microscopy, *Mech. Soft Mater.* 2 (1) (2020) 6, doi:[10.1007/s42558-020-00021-8](https://doi.org/10.1007/s42558-020-00021-8).
- [33] E. Brazulius, M. Diezi, T. Biedermann, L. Pontiggia, M. Schmucki, F. Hartmann-Fritsch, J. Luginbühl, C. Schiestl, M. Meuli, E. Reichmann, Modified plastic compression of collagen hydrogels provides an ideal matrix for clinically applicable skin substitutes, *Tissue Eng. Part C Methods* 18 (6) (2012) 464–474, doi:[10.1089/ten.tec.2011.0561](https://doi.org/10.1089/ten.tec.2011.0561).
- [34] C. Morin, C. Hellmich, P. Henits, Fibrillar structure and elasticity of hydrating collagen: a quantitative multiscale approach, *J. Theor. Biol.* 317 (2013) 384–393, doi:[10.1016/j.jtbi.2012.09.026](https://doi.org/10.1016/j.jtbi.2012.09.026).
- [35] R.L. Mauck, M.A. Soltz, C.C.B. Wang, D.D. Wong, P.-H.G. Chao, W.B. Valhmu, C.T. Hung, G.A. Ateshian, Functional tissue engineering of articular cartilage through dynamic loading of chondrocyte-seeded agarose gels, *J. Biomech. Eng.* 122 (3) (2000) 252–260, doi:[10.1115/1.429656](https://doi.org/10.1115/1.429656).
- [36] S.T. Kreger, S.L. Voytik-Harbin, Hyaluronan concentration within a 3D collagen matrix modulates matrix viscoelasticity, but not fibroblast response, *Matrix Biol.* 28 (6) (2009) 336–346, doi:[10.1016/j.matbio.2009.05.001](https://doi.org/10.1016/j.matbio.2009.05.001).
- [37] D.C. Lin, E.K. Dimitriadis, F. Horkay, Robust strategies for automated AFM force curve analysis—I. Non-adhesive indentation of soft, inhomogeneous materials, *J. Biomech. Eng.* 129 (3) (2007) 430, doi:[10.1115/1.2720924](https://doi.org/10.1115/1.2720924).
- [38] A. Wahlsten, *Multiscale mechanics of skin and skin-equivalent materials*, ETH Zurich, 2022 Ph.D. Thesis.
- [39] C. Flynn, A. Taberner, P. Nielsen, Mechanical characterisation of in vivo human skin using a 3D force-sensitive micro-robot and finite element analysis, *Biomech. Model. Mechanobiol.* 10 (1) (2011) 27–38, doi:[10.1007/s10237-010-0216-8](https://doi.org/10.1007/s10237-010-0216-8).
- [40] S. Diridollou, F. Patat, F. Gens, L. Vaillant, D. Black, J.M. Lagarde, Y. Gall, M. Berson, In vivo model of the mechanical properties of the human skin under suction, *Skin Res. Technol.* 6 (4) (2000) 214–221, doi:[10.1034/j.1600-0846.2000.006004214.x](https://doi.org/10.1034/j.1600-0846.2000.006004214.x).
- [41] A.E. Ehret, K. Bircher, A. Stracuzzi, V. Marina, M. Zündel, E. Mazza, Inverse poroelasticity as a fundamental mechanism in biomechanics and mechanobiology, *Nat. Commun.* 8 (1) (2017) 1–9, doi:[10.1038/s41467-017-00801-3](https://doi.org/10.1038/s41467-017-00801-3).
- [42] A. Stracuzzi, *Chemomechanical interactions in biomaterials: multiphase and multiscale analyses*, ETH Zurich, 2020 Ph.D. Thesis.
- [43] A. Mauri, R. Hopf, A.E. Ehret, C.R. Picu, E. Mazza, A discrete network model to represent the deformation behavior of human amnion, *J. Mech. Behav. Biomed. Mater.* 58 (2016) 45–56, doi:[10.1016/j.jmbbm.2015.11.009](https://doi.org/10.1016/j.jmbbm.2015.11.009).
- [44] N.I. Fisher, T. Lewis, B.J.J. Embleton, *Statistical analysis of spherical data*, Cambridge University Press, 1987, doi:[10.1017/CBO9780511623059](https://doi.org/10.1017/CBO9780511623059).
- [45] K. Mardia, *Distributions on spheres*, in: *Statistics of Directional Data*, Academic Press, 1972, pp. 212–248, doi:[10.1016/B978-0-12-471150-1.50014-5](https://doi.org/10.1016/B978-0-12-471150-1.50014-5).

- [46] W. Ehlers, N. Karajan, B. Markert, An extended biphasic model for charged hydrated tissues with application to the intervertebral disc, *Biomech. Model. Mechanobiol.* 8 (3) (2009) 233–251, doi:10.1007/s10237-008-0129-y.
- [47] R.C. Picu, S. Deogekar, M.R. Islam, Poisson's contraction and fiber kinematics in tissue: Insight from collagen network simulations, *J. Biomech. Eng.* 140 (2) (2018) 021002, doi:10.1115/1.4038428.
- [48] N. Nakagawa, M. Matsumoto, S. Sakai, In vivo measurement of the water content in the dermis by confocal raman spectroscopy, *Ski. Res. Technol.* 16 (2) (2010) 137–141, doi:10.1111/j.1600-0846.2009.00410.x.
- [49] G.D. Weinstein, R.J. Boucek, Collagen and elastin of human dermis, *J. Invest. Dermatol.* 35 (4) (1960) 227–229, doi:10.1038/jid.1960.109.
- [50] I.A. Brown, Scanning electron microscopy of human dermal fibrous tissue, *J. Anat.* 113 (Pt 2) (1972) 159–168.
- [51] M. Pensalfini, A.E. Ehret, S. Stüdeli, D. Marino, A. Kaech, E. Reichmann, E. Mazza, Factors affecting the mechanical behavior of collagen hydrogels for skin tissue engineering, *J. Mech. Behav. Biomed. Mater.* 69 (2017) 85–97, doi:10.1016/j.jmbbm.2016.12.004.
- [52] V. Kouznetsova, Computational homogenization for the multi-scale analysis of multi-phase materials, Eindhoven University of Technology, 2002 Ph.D. Thesis.
- [53] U.S. Schwarz, S.A. Safran, Physics of adherent cells, *Rev. Mod. Phys.* 85 (3) (2013) 1327–1381, doi:10.1103/RevModPhys.85.1327.
- [54] F. Beroz, L.M. Jawerth, S. Münster, D.A. Weitz, C.P. Broedersz, N.S. Wingreen, Physical limits to biomechanical sensing in disordered fibre networks, *Nat. Commun.* 8 (1) (2017) 16096, doi:10.1038/ncomms16096.
- [55] C.J. Boyle, M. Plotczyk, S.F. Villalta, S. Patel, S. Hettiaratchy, S.D. Masouros, M.A. Masen, C.A. Higgins, Morphology and composition play distinct and complementary roles in the tolerance of plantar skin to mechanical load, *Sci. Adv.* 5 (10) (2019) eaay0244, doi:10.1126/sciadv.aay0244.
- [56] A.P. Kao, J.T. Connelly, A.H. Barber, 3D Nanomechanical evaluations of dermal structures in skin, *J. Mech. Behav. Biomed. Mater.* 57 (2016) 14–23, doi:10.1016/j.jmbbm.2015.11.017.
- [57] T. Jee, K. Komvopoulos, In vitro measurement of the mechanical properties of skin by nano/microindentation methods, *J. Biomech.* 47 (5) (2014) 1186–1192, doi:10.1016/j.jbiomech.2013.10.020.
- [58] X. Liang, S.A. Boppert, Biomechanical properties of in vivo human skin from dynamic optical coherence elastography, *IEEE Trans. Biomed. Eng.* 57 (4) (2010) 953–959, doi:10.1109/TBME.2009.2033464.
- [59] A. Mauri, A.E. Ehret, D.S.A. De Focatiis, E. Mazza, A model for the compressible, viscoelastic behavior of human amnion addressing tissue variability through a single parameter, *Biomech. Model. Mechanobiol.* 15 (4) (2016) 1005–1017, doi:10.1007/s10237-015-0739-0.
- [60] K. Bircher, A.E. Ehret, E. Mazza, Mechanical characteristics of bovine Glisson's capsule as a model tissue for soft collagenous membranes, *J. Biomech. Eng.* 138 (8) (2016) 081005, doi:10.1115/1.4033917.
- [61] P. Dutov, O. Antipova, S. Varma, J.P.R.O. Orgel, J.D. Schieber, Measurement of elastic modulus of collagen type I single fiber, *PLoS One* 11 (1) (2016) e0145711, doi:10.1371/journal.pone.0145711.
- [62] I. Brown, A scanning electron microscope study of the effects of uniaxial tension on human skin, *Br. J. Dermatol.* 89 (4) (1973) 383–393, doi:10.1111/j.1365-2133.1973.tb02993.x.
- [63] R.A. Brown, In the beginning there were soft collagen-cell gels: towards better 3D connective tissue models? *Exp. Cell Res.* 319 (16) (2013) 2460–2469, doi:10.1016/j.yexcr.2013.07.001.
- [64] B. Zavan, R. Cortivo, G. Abatangelo, Hydrogels and tissue engineering, in: R. Barbucci (Ed.), *Hydrogels. Biological Properties and Applications*, Springer Milan, 2009, pp. 1–8, doi:10.1007/978-88-470-1104-5_1.
- [65] D.L. Matera, K.M. DiLillo, M.R. Smith, C.D. Davidson, R. Parikh, M. Said, C.A. Wilke, I.M. Lombaert, K.B. Arnold, B.B. Moore, B.M. Baker, Microengineered 3D pulmonary interstitial mimetics highlight a critical role for matrix degradation in myofibroblast differentiation, *Sci. Adv.* 6 (37) (2020) eabb5069, doi:10.1126/sciadv.abb5069.
- [66] K. Ghosh, Z. Pan, E. Guan, S. Ge, Y. Liu, T. Nakamura, X.D. Ren, M. Rafailovich, R.A. Clark, Cell adaptation to a physiologically relevant ECM mimic with different viscoelastic properties, *Biomaterials* 28 (4) (2007) 671–679, doi:10.1016/j.biomaterials.2006.09.038.
- [67] J.P. Winer, P.A. Janmey, M.E. McCormick, M. Funaki, Bone marrow-derived human mesenchymal stem cells become quiescent on soft substrates but remain responsive to chemical or mechanical stimuli, *Tissue Eng. Part A* 15 (1) (2009) 147–154, doi:10.1089/ten.tea.2007.0388.
- [68] A. Engler, L. Bacakova, C. Newman, A. Hategan, M. Griffin, D. Discher, Substrate compliance versus ligand density in cell on gel responses, *Biophys. J.* 86 (1) (2004) 617–628, doi:10.1016/S0006-3495(04)74140-5.
- [69] S. Asano, S. Ito, K. Takahashi, K. Furuya, M. Kondo, M. Sokabe, Y. Hasegawa, Matrix stiffness regulates migration of human lung fibroblasts, *Physiol. Rep.* 5 (9) (2017) e13281, doi:10.14814/phy2.13281.
- [70] Y. Osada, J. Ping Gong, Y. Tanaka, Polymer gels, *J. Macromol. Sci. Part C Polym. Rev.* 44 (1) (2004) 87–112, doi:10.1081/MC-120027935.
- [71] O. Chaudhuri, J. Cooper-White, P.A. Janmey, D.J. Mooney, V.B. Shenoy, Effects of extracellular matrix viscoelasticity on cellular behaviour, *Nature* 584 (7822) (2020) 535–546, doi:10.1038/s41586-020-2612-2.
- [72] K. Svoboda, S.M. Block, Biological applications of optical forces, *Annu. Rev. Biophys. Biomol. Struct.* 23 (1) (1994) 247–285, doi:10.1146/annurev.bb.23.060194.001335.
- [73] M. Tanase, N. Biais, M. Sheetz, Magnetic tweezers in cell biology, *Methods Cell Biol.* 83 (2007) 473–493, doi:10.1016/S0091-679X(07)83020-2.
- [74] D.O. Asgeirsson, M.G. Christiansen, T. Valentin, L. Somm, N. Mirkhani, A.H. Nami, V. Hosseini, S. Schuerle, 3D Magnetically controlled spatiotemporal probing and actuation of collagen networks from a single cell perspective, *Lab Chip* 21 (20) (2021) 3850–3862, doi:10.1039/D1LC00657F.